Title: Functional connectome through the human life span

Authors: Lianglong Sun[1,2,3], Tengda Zhao[1,2,3,#], Xinyuan Liang[1,2,3,#], Mingrui Xia[1,2,3,#], Qiongling Li[1,2,3], Xuhong Liao[4], Gaolang Gong[1,2,3,5], Qian Wang[1,2,3], Chenxuan Pang[1,2,3], Qian Yu[1,2,3], Yanchao Bi[1,2,3,5], Pindong Chen[6], Rui Chen[1], Yuan Chen[7], Taolin Chen[8], Jingliang Cheng[7], Yuqi Cheng[9], Zaixu Cui[5], Zhengjia Dai[1,2,3], Yao Deng[1], Yuyin Ding[1], Qi Dong[1], Dingna Duan[1,2,3], Jia-Hong Gao[10,11,12], Qiyong Gong[8,13], Ying Han[14], Zaizhu Han[1,3], Chu-Chung Huang[15], Ruiwang Huang[1,3], Ran Huo[16], Lingjiang Li[17,18], Ching-Po Lin[19,20,21], Qixiang Lin[1,2,3], Bangshan Liu[17,18],Chao Liu[1,3], Ningyu Liu[1], Ying Liu[16], Yong Liu[22], Jing Lu[1], Leilei Ma[1], Weiwei Men[10,11], Shaozheng Qin[1,2,3,5], Jiang Qiu[23,24], Shijun Qiu[25], Tianmei Si[26], Shuping Tan[27], Yanqing Tang[28], Sha Tao[1], Dawei Wang[29], Fei Wang[28], Jiali Wang[1], Pan Wang[30], Xiaoqin Wang[23,24], Yanpei Wang[1], Dongtao Wei[23,24], Yankun Wu[26], Peng Xie[31,32], Xiufeng Xu[9], Yuehua Xu[1,2,3], Zhilei Xu[1,2,3], Liyuan Yang[1,2,3], Huishu Yuan[16], Zilong Zeng[1,2,3], Haibo Zhang[1], Xi Zhang[33], Gai Zhao[1], Yanting Zheng[25], Suyu Zhong[22], Alzheimer's Disease Neuroimaging Initiative, Cam-CAN, Developing Human Connectome Project, DIDA-MDD Working Group, MCADI, NSPN, and Yong He[1,2,3,5,*]

Affiliations:

[1] State Key Laboratory of Cognitive Neuroscience and Learning, Beijing Normal University, Beijing, China;
[2] Beijing Key Laboratory of Brain Imaging and Connectomics, Beijing Normal University, Beijing, China;
[3] IDG/McGovern Institute for Brain Research, Beijing Normal University, Beijing, China;
[4] School of Systems Science, Beijing Normal University, Beijing, China;
[5] Chinese Institute for Brain Research, Beijing, China;
[6] Brainnetome Center & National Laboratory of Pattern Recognition, Institute of Automation, Chinese Academy of Sciences, Beijing, China;
[7] Department of Magnetic Resonance Imaging, The First Affiliated Hospital of Zhengzhou University, Zhengzhou, China;
[8] Huaxi MR Research Center (HMRRC), Department of Radiology, West China Hospital, Sichuan University, Chengdu, China;
[9] Department of Psychiatry, First Affiliated Hospital of Kunming Medical University, Kunming, China;
[10] Center for MRI Research, Academy for Advanced Interdisciplinary Studies, Peking University, Beijing, China;
[11] Beijing City Key Laboratory for Medical Physics and Engineering, Institute of Heavy Ion Physics, School of Physics, Peking University, Beijing, China;
[12] IDG/McGovern Institute for Brain Research, Peking University, Beijing, China;
[13] Research Unit of Psychoradiology, Chinese Academy of Medical Sciences, Chengdu, China;
[14] Department of Neurology, Xuanwu Hospital of Capital Medical University, Beijing, China;
[15] Key Laboratory of Brain Functional Genomics (Ministry of Education), Affiliated Mental Health Center (ECNU), School of Psychology and Cognitive Science, East China Normal University, Shanghai, China;
[16] Department of Radiology, Peking University Third Hospital, Beijing, China;
[17] Department of Psychiatry, and National Clinical Research Center for Mental Disorders, The Second Xiangya Hospital of Central South University, Changsha, China;
[18] Mental Health Institute of Central South University, China National Technology Institute on Mental Disorders, Hunan Technology Institute of Psychiatry, Hunan Key Laboratory of Psychiatry and Mental Health, Hunan Medical Center for Mental Health, Changsha, China;
[19] Institute of Science and Technology for Brain-Inspired Intelligence, Fudan University, Shanghai, China;
[20] Institute of Neuroscience, National Yang Ming Chiao Tung University, Taipei;
[21] Department of Education and Research, Taipei City Hospital, Taipei;
[22] Center for Artificial Intelligence in Medical Imaging, School of Artificial Intelligence, Beijing University of Posts and Telecommunications, Beijing, China;

[23] Key Laboratory of Cognition and Personality (SWU), Ministry of Education, Chongqing, China;
[24] Department of Psychology, Southwest University, Chongqing, China;
[25] Department of Radiology, The First Affiliated Hospital of Guangzhou University of Chinese Medicine, Guangzhou, China;
[26] Peking University Sixth Hospital, Peking University Institute of Mental Health, NHC Key Laboratory of Mental Health (Peking University), National Clinical Research Center for Mental Disorders (Peking University Sixth Hospital), Peking University, Beijing, China;
[27] Beijing Huilongguan Hospital, Peking University Huilongguan Clinical Medical School, Beijing, China;
[28] Department of Psychiatry, The First Affiliated Hospital of China Medical University, Shenyang, China;
[29] Department of Radiology, Qilu Hospital of Shandong University, Ji'nan, China;
[30] Department of Neurology, Tianjin Huanhu Hospital, Tianjin University, Tianjin, China;
[31] Chongqing Key Laboratory of Neurobiology, Chongqing, China;
[32] Department of Neurology, The First Affiliated Hospital of Chongqing Medical University, Chongqing, China;
[33] Department of Neurology, the Second Medical Centre, National Clinical Research Centre for Geriatric Diseases, Chinese PLA General Hospital, Beijing, China.

[#] These authors contributed equally

* Correspondence to: yong.he@bnu.edu.cn

Keywords: brain chart, brain atlas, connectomics, fMRI

Manuscript information: 33 text pages, 6 figures.
(Supplementary Information: 17 text pages, 14 figures, 2 tables.)

Abstract

The functional connectome of the human brain represents the fundamental network architecture of functional interdependence in brain activity, but its normative growth trajectory across the life course remains unknown. Here, we aggregate the largest, quality-controlled multimodal neuroimaging dataset from 119 global sites, including 33,809 task-free fMRI and structural MRI scans from 32,328 individuals ranging in age from 32 postmenstrual weeks to 80 years. Lifespan growth charts of the connectome are quantified at the whole cortex, system, and regional levels using generalized additive models for location, scale, and shape. We report critical inflection points in the non-linear growth trajectories of the whole-brain functional connectome, particularly peaking in the fourth decade of life. Having established the first fine-grained, lifespan-spanning suite of system-level brain atlases, we generate person-specific parcellation maps and further show distinct maturation timelines for functional segregation within different subsystems. We identify a spatiotemporal gradient axis that governs the life-course growth of regional connectivity, transitioning from primary sensory cortices to higher-order association regions. Using the connectome-based normative model, we demonstrate substantial individual heterogeneities at the network level in patients with autism spectrum disorder and patients with major depressive disorder. Our findings shed light on the life-course evolution of the functional connectome and serve as a normative reference for quantifying individual variation in patients with neurological and psychiatric disorders.

Introduction

The resting human brain, characterized by intrinsic or spontaneous cortical-cortical interactions, has been increasingly understood through the perspective of the connectome over the past two decades [1-5]. The emergence, development, and aging of intrinsic connectome architecture enable the dynamic reorganization of functional specialization and integration throughout the entire lifespan, contributing to continuous changes in human cognition and behavior [6-9]. Understanding the spatiotemporal growth process in the typical functional connectome is critical for grasping network-level evolving principles in healthy individuals and pinpointing periods of heightened vulnerability or potential. Disruption of these normative connectome patterns, especially during specific time windows, can predispose individuals to a spectrum of neurodevelopmental [10-12], neurodegenerative [13], and psychiatric disorders [14-16]. The growth chart framework offers an invaluable tool for charting normative reference curves in the human brain [17-20]. Very recently, Bethlehem et al. [18] delineated the life-cycle growth curves of brain morphometry by aggregating the largest multi-site structural MRI dataset to date (123,984 scans from 101,457 human participants), marking a significant stride toward reproducible and generalizable brain charts. However, it remains unknown about the normative growth trajectory of functional brain connectome over the human life course.

Previous studies employing task-free functional MRI (fMRI) data have reported the age-related characteristics of the functional connectome [21-23]. However, most of these investigations were limited to specific growth stages with narrow age intervals. For instance, data from perinatal and early postnatal periods (e.g., 0-6 years) are rarely integrated into studies involving childhood, adolescence, and adulthood; thus, the opportunity to depict continuous life-cycle dynamic evolution from gestation through older age is lost. Although a few studies have attempted to encompass a broader age range from the childhood stage to late adulthood, they suffered from challenges to robust estimation of normative growth curves due to limited sample sizes (usually < 1,000) [24-29]. Moreover, there are great inconsistencies in the literature regarding functional connectivity trajectories, with no consensus emerging on the developmental directions and growth milestones. Specifically, Cao et al. [25] reported the peak of global functional connectivity across the entire brain at approximately 30 years of age, while other investigations suggest earlier peaks [24] or depict a continuous decline over the lifespan [30]. Divergent trends were observed for sensorimotor regions, with reports showing ascending [31], descending [32], and stable [33] developmental trajectories from childhood to adolescence. Similarly, connectivity patterns between the default and frontoparietal networks have been reported to both increase [34] and decrease [35, 36] during this phase. Such result discrepancies across studies are probably due to the pronounced sensitivity of high-dimensional fMRI data to variation in scanner platforms and sequences, image quality, data processing and statistical methods, as well as the cohort's population heterogeneity [6]. This highlights the paramount importance of large sample sizes, rigorous data quality control processes, unified data processing protocols, and standardized statistical modeling frameworks in accurately characterizing growth curves of the life-course functional connectome.

To address this gap, we aggregated the largest and rigorously quality-controlled multimodal neuroimaging dataset across 119 global sites, consisting of 33,809 task-free fMRI and structural MRI scans from 32,328 individuals ranging in age from 32 postmenstrual weeks to 80 years. We undertook a comprehensive network modeling analysis to delineate the non-linear trajectories of

the functional connectome across multiple scales. We began by characterizing the lifespan changes and the rates of changes in the overall patterns of the whole-brain functional connectome, uncovering important life-course milestones. Subsequently, we established the first set of continuous age-related, system-level atlases across the lifespan and provided an unreported portrayal of the distinct growth patterns across brain systems. Next, we sought to elucidate the spatiotemporal principles governing connectome growth at a finer vertex-level resolution. Finally, to explore the potential clinical application of our life-course normative model, we presented a multiscale characterization to quantify the heterogeneity of participants with autism spectrum disorder (ASD) (N = 653) and major depressive disorder (MDD) (N = 622) using individualized deviation scores.

Results

We initially collected 45,525 scans from 43,377 participants with multimodal structural MRI and task-free fMRI data in total. After a stringent quality control process (for details, see the Methods and Supplementary Fig. 1), we obtained a final sample of 35,084 scans with high-quality imaging data, which included 33,809 scans of healthy individuals (N = 32,328) and 1,275 scans of patients (N = 1,275) (Fig. 1a). For the detailed acquisition parameters and demographics of the datasets, see Supplementary Table 1. Using the standardized and highly unified processing pipeline (Methods and Supplementary Fig. 2), for each individual we obtained the surface-based preprocessed blood oxygenation level-dependent (BOLD) signals in fsaverage4 space (4,661 vertices in total). Then, we constructed a vertex-wise 4,661×4,661 functional connectome matrix by calculating the Pearson correlation coefficient between the time courses of each vertex. Fig. 1b illustrates the functional connectome matrices of representative subjects at various age points. Then, we comprehensively examined the individual connectome at the whole-brain, system, and regional levels, harmonizing all measures across sites. Guided by the recommendations from the World Health Organization [37], we utilized generalized additive models for location, scale, and shape (GAMLSS) [37, 38] to elucidate the age-related non-linear trajectories for healthy populations, with sex and in-scanner head motion as fixed effects. GAMLSS offers a robust framework for modeling non-linear growth charts and is widely employed in neurodevelopmental studies [18, 39-41]. To evaluate the rate of change (velocity) and inflection points, we calculated the first derivatives of the trajectories. Detailed GAMLSS specification, model estimation, and sensitivity analyses of model stability and robustness are presented in the Methods.

Mapping normative growth of the whole-brain functional connectome over the lifespan

To provide basic developmental and aging insight into the overall functional connectome, we first characterized the normative trajectories of global mean and variance (estimated by standard deviation) of the whole-brain connectome matrix. The lifespan curve of the mean functional connectivity across the entire brain (Fig. 1c) showed a non-linear increase from 32 postmenstrual weeks onward, peaking at 40.0 years (95% bootstrap confidence interval (CI) 39.4-40.5), followed by a subsequent non-linear decline. The peak of the increased growth rate occurred at 18.0 years (95% bootstrap CI 15.1-20.2), while the maximum rate of decline was observed at 57.4 years (95% bootstrap CI 55.8-59.8). The global variance in whole-brain functional connectivity (Fig. 1d) also exhibited a non-linear growth pattern, peaking in adulthood at 34.7 years (95% bootstrap CI 33.0-36.4), with maximum rates of increase and decline occurring at 32

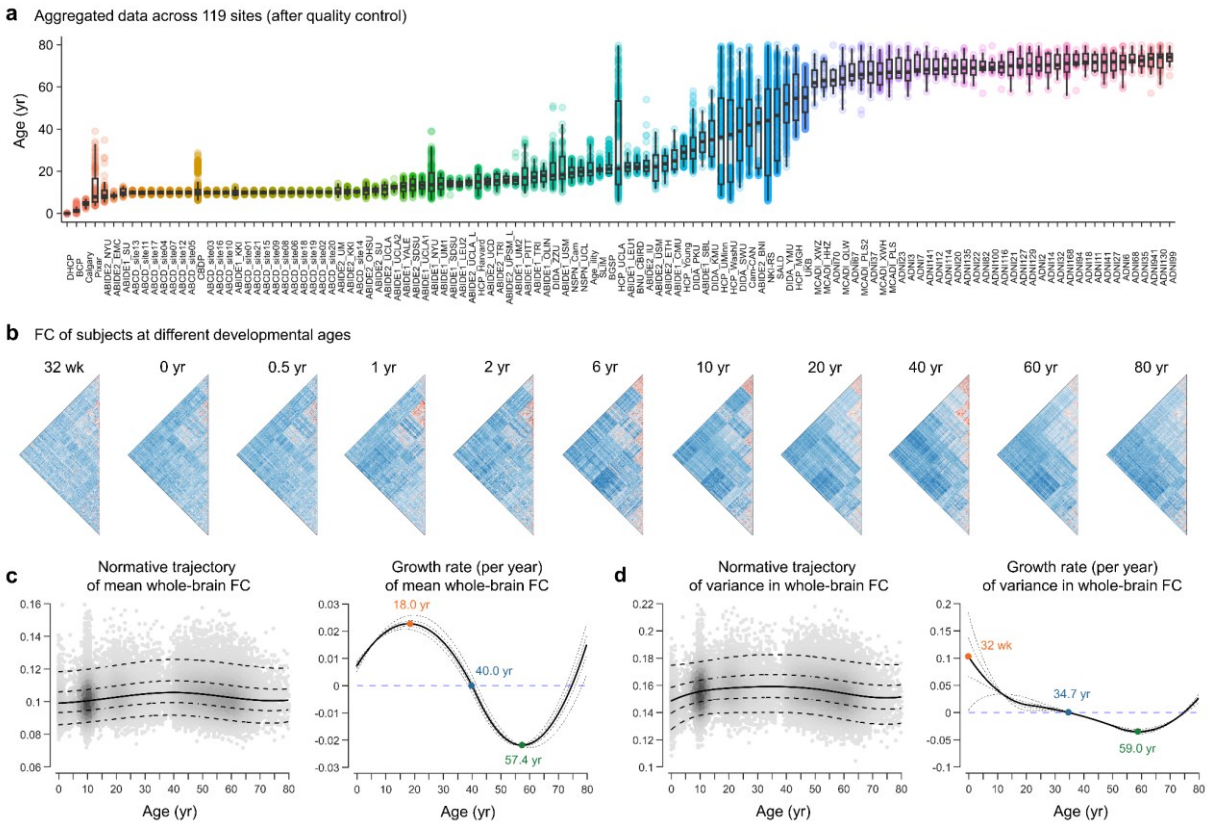

Fig. 1 | Data samples, functional connectome, and global growth of the connectome over the lifespan. a, Quality-controlled MRI data from 119 scanning sites comprising 35,084 scans (N = 33603) of individuals who collectively spanned the age range from 32 postmenstrual weeks to 80 years. Box plots show the age distribution of individuals for each site of data acquisition. Detailed acquisition parameters and demographics of each site are provided in Supplementary Table 1. **b**, The functional connectivity (FC) matrices of representative subjects at different developmental ages. **c**, Normative trajectory (left panel) and growth rate (right panel) of whole-brain mean FC as estimated by GAMLSS. The median (50% centile) is represented by a solid line, while the 5%, 25%, 75%, and 95% centiles are indicated by dotted lines. The growth velocity is characterized by the first derivative of the trajectory. Critical milestones in the lifespan developmental trajectory include a stabilization of growth rate at 40.0 years (95% bootstrap confidence interval (CI) 39.4-40.5), a maximum increase at 18.0 years (95% bootstrap CI 15.1-20.2), and a maximum decline at 57.4 years (95% bootstrap CI 55.8-59.8). **d**, Normative trajectory and growth rate of variance in whole-brain FC, with a peak age at 34.7 years (95% bootstrap CI 33.0-36.4), a maximum increase occurring at 32 postmenstrual weeks (95% bootstrap CI 32 week-32 week), and a maximum decline occurring at 59.0 years (95% bootstrap CI 57.8-61.1). wk, week; mon, month; yr, year.

postmenstrual weeks (95% bootstrap CI 32 week-32 week) and 59.0 years (95% bootstrap CI 57.8-61.1), respectively. These non-linear trajectories signified that whole-brain connection strength and connection diversity evolve in a temporally coordinated manner across the lifespan.

Lifespan growth of system-specific cortical organization in the functional connectome

Functional segregation and integration are two fundamental organizational principles of human brain connectomes [1]. To understand lifespan growth patterns of functional segregation and integration, we established the normative trajectories of functional connectome at the system

level. The initial step entailed parcellating the cortical cortex into distinct functional systems for each individual. Convergent evidence has demonstrated that relying on population-level atlases for individual analysis disregards the crucial intersubject variability in functional topography organization [42-45]. Such oversight leads to misinterpretation of spatial distribution differences as system-level disparities [43, 46], thereby risking inaccuracies in mapping both intra- and inter-system connectivity. Moreover, although prior studies on fetal and infant brains have illuminated the early emergence of basic forms of large-scale functional systems, including visual [47-50], somatomotor [47-50], dorsal attention [51, 52], ventral attention [47], frontoparietal [48, 50, 52], and default mode networks [47-50, 52], the functional architecture of an individual's system undergoes dramatic refinement and reorganization throughout the protracted life course [21, 53]. To enhance the precision of constructing individual-specific functional networks, it is imperative to establish a series of continuous growth atlases with accurate system correspondences over the life course.

To address this issue, here we proposed a Gaussian-weighted iterative age-specific group atlas (GIAGA) generation approach (Methods and Supplementary Fig. 3a). Central to this approach is the iterative refinement process: Yeo's adult atlas [54] was utilized as a prior to generate personalized parcellation for each participant in a given age group. Subsequently, these personalized parcellations were aggregated to construct an age-specific population-level atlas, wherein the participants' contribution was weighted according to their age's position within a Gaussian probability distribution. This process was reiterated until the age-specific population-level atlas converged. By dividing participants from 32 postmenstrual weeks to 80 years into 26 distinct age groups, we established the first set of age-specific brain atlases that cover the lifespan (Fig. 2a). Each of the 26 brain atlases was parcellated into seven canonical functional networks. For each network, we calculated the network size ratio, measured by the proportion of vertices, and the distributed score, defined by the number of spatially discontinuous subregions (Fig. 2b). We noted that the default mode (DM), frontoparietal (FP), and ventral attention (VA) networks exhibited a slight expansion in network size during the first month of life, while their distribution scores developed until late childhood. In contrast, the somatomotor (SM), visual (VIS), and dorsal attention (DA) networks displayed a relatively stable pattern in network size and network discretization throughout the lifespan. To quantify the growth patterns of the whole-brain atlas and across diverse networks, we computed the network similarity using the overlay index and Dice coefficient between each atlas and the designated reference atlas (Methods). Here, the reference atlas was derived from the average of several adult-like atlases (spanning from the 18- to 70-year atlas) that exhibited high alignment due to clustering (Methods and Supplementary Fig. 5). We found that the whole-brain atlas similarity rapidly increased during the first two decades of life and plateaued before declining in old age (Fig. 2c). At the system level, we noted that both the VIS and SM networks displayed adult-resembling patterns (similarity of 80%) in neonate stages, whereas DM, FP, DA, and VA networks developed adult-resembling patterns (similarity of 80%) at age 4 (Fig. 2d and 2e). To map individual-specific functional systems for each participant, we leveraged an iterative parcellation procedure (Supplementary Fig. 3b) proposed by Wang et al. [55] which has been proven to accurately identify personalized functional networks in healthy [43, 55] and diseased individuals [56-58]. Consistent with the developmental pattern of the age-specific atlas, the normative growth trajectories revealed that individualized atlas similarity with the reference increased from 32 postmenstrual weeks, peaking at 30.0 years (95% bootstrap CI 29.2-30.7); keeping a stable level to 54 years (95% bootstrap CI 53.0-56.0) and then decline accelerated continuously until 80 years of age (Fig. 2f and 2g).

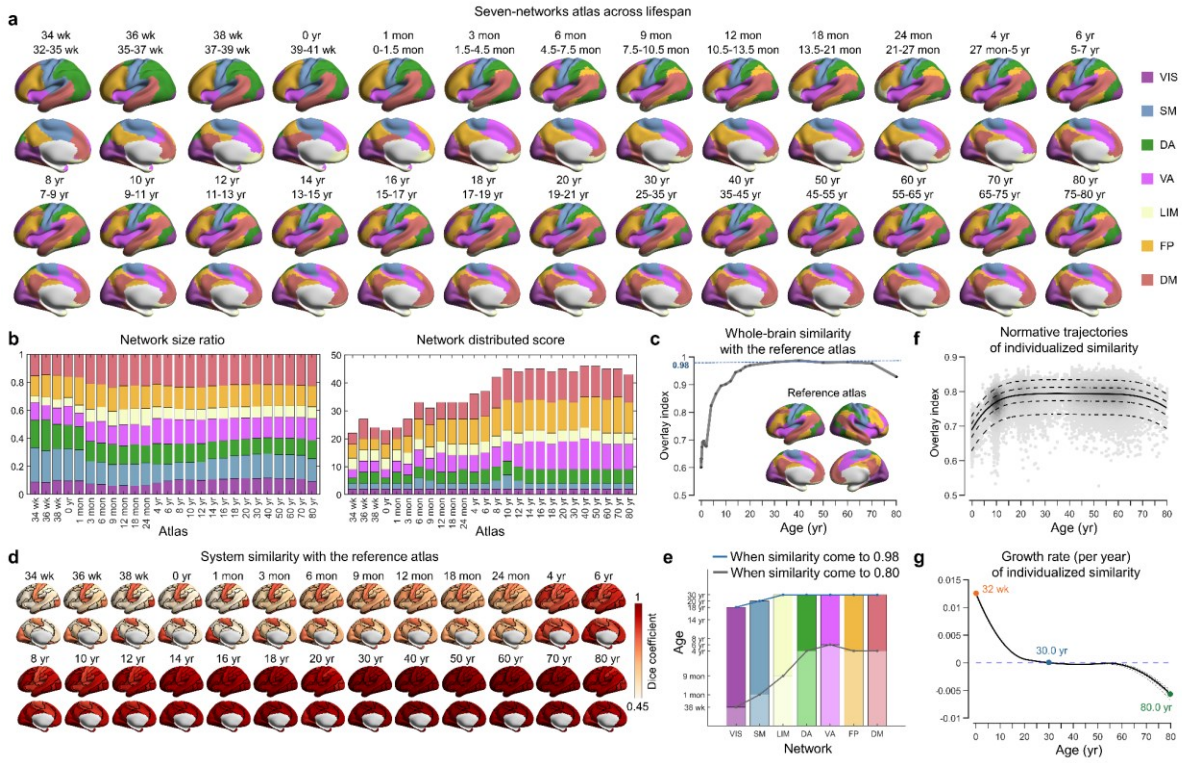

Fig. 2 | Population-level and individual-level functional atlases throughout the lifespan. a, Employing the Gaussian-weighted iterative group atlas generation approach (for details, see Methods and Supplementary Fig. 3), the first life-cycle set of functional seven-network atlases from 32 postmenstrual weeks to 80 years was established (26 atlases in total). Only the left hemisphere is displayed here; for the full-brain atlas, refer to Supplementary Fig. 4. Labels of each system were mapped into the HCP fs_LR_32k surface and visualized using BrainNet Viewer [60]. **b**, Network size ratio and network distributed score of each system in all developmental atlases. The network size ratio was calculated as the vertex number of the system divided by the total cortical vertex number. The network distributed score was measured by the spatially discontinuous subregion (≥ 5 vertices) number of the system. **c**, Whole-brain similarity of each age-specific atlas with the reference atlas. **d**, System similarity of each age-specific atlas with the corresponding system in the reference atlas. **e**, The age when the system similarity of each age-specific atlas reaches 0.8 and 0.98. **f-g**, Normative trajectory and growth rate of individualized atlas similarity with the reference atlas. The similarity increased from 32 postmenstrual weeks, peaking at 30.0 years (95% bootstrap CI 29.2-30.7), and undergoing a continually accelerated decline starting at approximately 54 years (95% bootstrap CI 53.0-56.0) until 80 years of age. VIS, visual; SM, somatomotor; DA, dorsal attention; VA, ventral attention; LIM, limbic; FP, frontoparietal; DM, default mode. wk, week; mon, month; yr, year.

We characterized the growth trajectories of within-system connectivity (functional segregation) and between-system connectivity (functional integration) (Supplementary Fig. 6) by leveraging person-specific network assignments. To further quantify the differences in the within-system connectivity in relation to the between-system connectivity, for each brain system we calculated the system segregation index [59]. This index measures the difference between mean within-system connectivity and mean between-system connectivity as a proportion of mean within-system connectivity [59] (Methods). Intriguingly, the whole-brain system segregation across all systems peaked at 23.5 years (95% bootstrap CI 20.7-24.3) and showed a more significant accelerated

decline around the sixth decade of life (Fig. 3a). At the system level, the primary VIS network consistently showcased the largest segregation throughout all age points (Fig. 3b), suggesting that the VIS network is more efficient in its in-network communication and relatively less integrated in its cross-network communication compared to other systems. Notably, distinct networks manifested heterochronous growth patterns (Fig. 3b and 3c). The VIS and DA networks exhibited similar life-cycle trajectories, both peaking early at approximately 10-11 years of age (VIS peak at 11.3 years (95% bootstrap CI 10.8-11.7); DA peak at 9.8 years (95% bootstrap CI 9.4-10.1)). Conversely, the DM and FP networks reached their peak late in the fourth decade (34.3 years, 95% bootstrap CI 29.6-57.8) and sixth decade (53.9 years, 95% bootstrap CI 48.3-57.3), respectively. Other networks reach their inflection points between late adolescence and early adulthood. In addition, the quantitative analysis of the growth rate illuminated that growth in the DM and FP networks increased faster in the early stages of neurodevelopment and declined faster in the late stages of senescence (Fig. 3b and 3d).

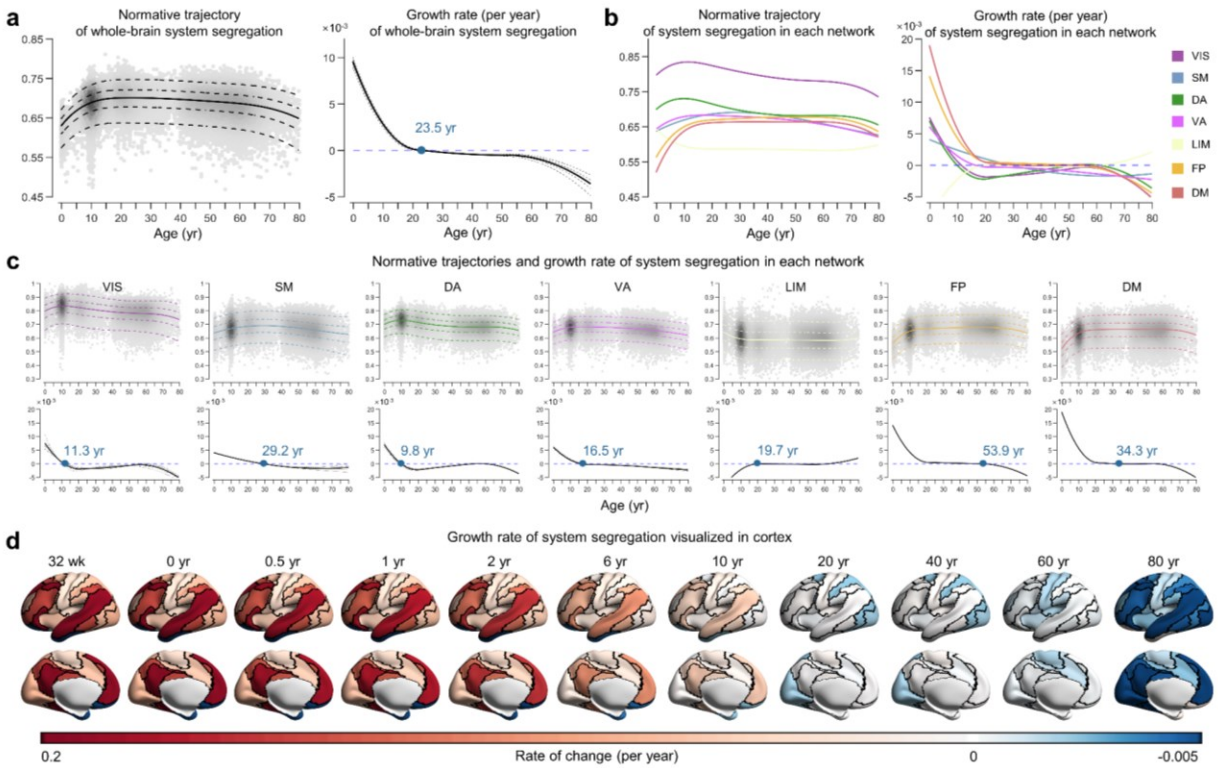

Fig. 3 | Life-course normative trajectories of individualized brain system segregation. a, Normative trajectory and growth rate of whole-brain system segregation. The developmental peak occurred at 23.5 years (95% bootstrap confidence interval 20.7-24.3). **b-c**, Normative trajectory and growth rate of system segregation for each network. The median (50% centile) is represented by a solid line, while the 5%, 25%, 75%, and 95% centiles are indicated by dotted lines. Developmental inflection points are marked in blue font. **d**, Growth rate of system segregation visualized in the cortex, with black lines depicting system boundaries. Values of each system are mapped and visualized in the HCP fs_LR_32k surface. VIS, visual; SM, somatomotor; DA, dorsal attention; VA, ventral attention; LIM, limbic; FP, frontoparietal; DM, default mode. wk, week; mon, month; yr, year.

Lifespan growth of regional-level functional connectivity reveals a spatial gradient pattern

Having identified distinct growth trajectories across various brain systems, we further explored the more nuanced spatial-temporal developmental patterns of the functional connectome at the regional level. First, we charted the normative trajectory of each vertex's functional connectivity strength (FCS) by calculating the average connectivity with all other vertices. Fig. 4a presents the trajectories for several vertices located in diverse brain regions, and Fig. 4b shows the fitted FCS and its growth rate across the cortex. Notably, the most pronounced changes in regional-level functional connectivity occurred within the first decade of life. Subsequently, we sought to elucidate how the entire growth trajectories spatially varied across the cortical cortex by mapping the primary spatial axis of FCS development. To this end, we utilized a principal component analysis (PCA) on the zero-centered 50% centiles of growth curves. The first PC, accounting for 66% of the variance, could be identified as the dominant axis of regional functional connectivity development (Fig. 4c). This axis captured a hierarchical spatial transition, commencing from primary sensorimotor and visual cortices and culminating in higher-order association regions, including the angular gyrus, precuneus, temporal, and prefrontal cortices. To illustrate the spatial-temporal pattern of developmental trajectories throughout the cortex more clearly, we segmented the principal developmental axis into 20 equal bins and averaged the trajectories for vertices within each bin. A continuous spectrum of trajectories along the life-cycle axis is presented in Fig. 4d.

The cortical landscape of the human brain is organized by a foundational gradient known as the sensorimotor-association (S-A) axis [61]. This axis spans from primary cortices, which are crucial for sensory and motor functions, to advanced transmodal regions responsible for complex cognitive and socio-emotional tasks. It has been widely shown to be instrumental in shaping neurodevelopmental processes [62-64]. Here, we aimed to investigate the extent to which our defined developmental axis aligns with the classical S-A axis as formulated by Sydnor et al [62]. (Fig. 4e). Utilizing a spin-based spatial permutation test [65], we found a significant association between the life-course principal growth axis and the S-A axis ($r = 0.67$; $P_{spin} < 0.0001$) (Fig. 4f). This finding suggested that canonical sensorimotor-association organization exerts a profound influence on the spatiotemporal growth of functional connectome throughout the human lifespan.

Sexual differences in lifespan trajectories

Sexual difference is increasingly recognized for its significant impact on brain development and aging [66, 67]. In GAMLSS modeling, we included a sex effect as another feature for establishing lifespan trajectories. The sex-stratified growth curves for individual metrics of the functional connectome are illustrated in Supplementary Fig. 7. These curves offer profound insights into the similar and distinct sex-dependent effects on the brain's functional connectome across the lifespan. Generally, both males and females showed similar non-linear lifespan growth curves in multiple metrics of functional connectome. However, some differences were also observed. Specifically, the global mean connectivity was higher in males than females, validating and broadening conclusions from previous studies confined to restricted age ranges [68, 69]. While females displayed higher global system segregation, particularly in adulthood. At the system level, females presented higher system segregation in the DM and VA networks and lower system segregation in the SM and limbic (LIM) networks throughout the lifespan as compared to males.

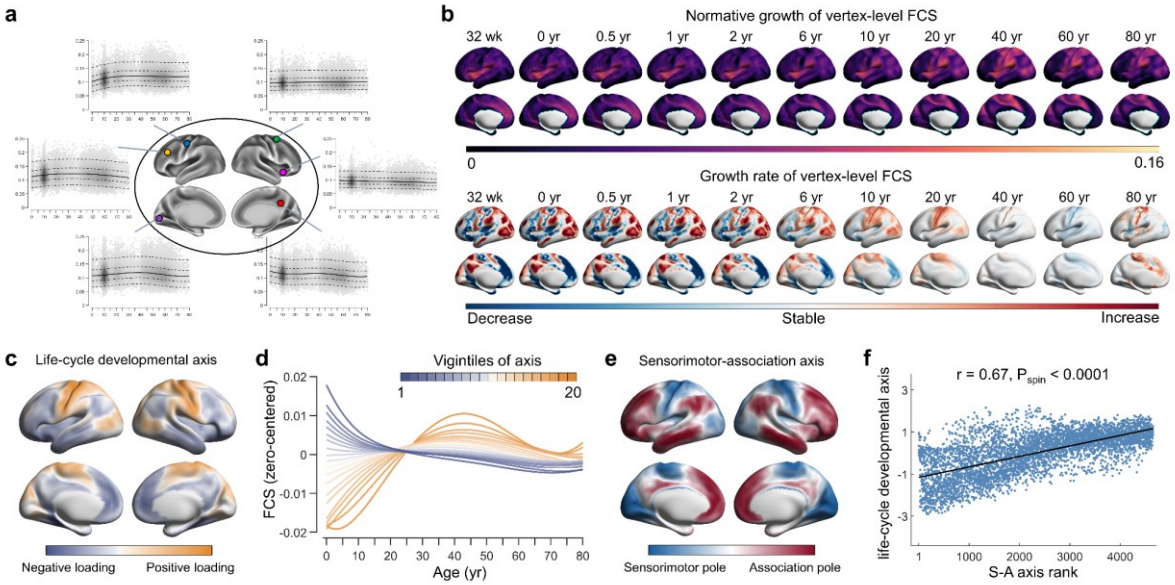

Fig. 4 | Lifespan normative trajectories of regional functional connectivity strength (FCS). a, Normative trajectories of example vertices from different regions. **b**, The fitted 50% centiles (top panel) and their growth rates (bottom panel) for all vertices at several key age points. **c**, The life-course developmental axis of brain functional connectivity, represented by the first principal component from a PCA on vertex-level FCS trajectories. **d**, Based on the lifespan principal axis, all vertices across the brain were equally divided into 20 bins. The zero-centered trajectories of all vertices within each bin were averaged. The first vigintile (depicted in darkest yellow) represents one pole of the axis, while the twentieth vigintile represents the opposite pole (depicted in darkest blue). The patterns of developmental trajectories vary continuously along the axis, with the greatest differences observed between the two poles. **e,** The sensorimotor-association (S-A) axis, as formulated by Sydnor et al. [62], represents a cortical continuum that transitions from primary regions to transmodal areas. **f,** A strong correlation was observed between the life-course principal developmental axis and the S-A axis ($r = 0.67$; $P_{spin} < 0.0001$) (linear association shown with a 95% confidence interval). All brain maps were mapped to the HCP fs_LR_32k surface for visualization. wk, week; mon, month; yr, year.

Identifying individual variation in brain disorders using connectome-based normative models

Recent literature has underscored the potential of normative models in disentangling the inherent heterogeneity in clinical cohorts by affording statistical inferences at the individual level [18, 70-76]. By benchmarking individual brain phenotypes against population-based standards, this approach allows for the quantification of individualized deviations from normative expectations, providing unique insights into the typicality or atypicality of each individual's brain structure or function. Based on the GAMLSS modeling framework, we comprehensively characterized the individualized deviation z score (age- and sex-specific) of each functional metric at the whole-brain, system, and regional levels in MDD patients (N = 622) and ASD patients (N = 653) (Methods). Deviation scores for healthy individuals were assessed using a 10-fold cross-validation strategy. The extreme deviations were defined as $z > |2.6|$ (corresponding to a $p < 0.005$), consistent with the criteria employed in prior studies [70, 71, 73].

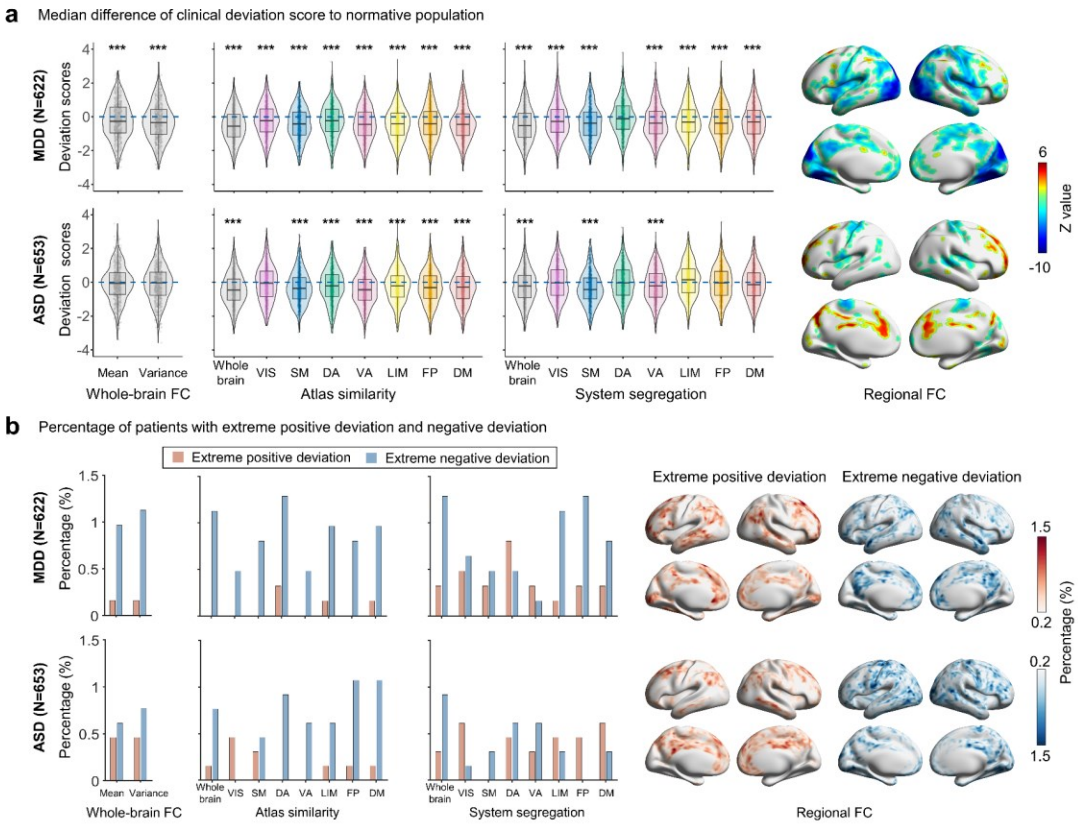

Fig. 5 | Individual variations of multiple connectome metrics in MDD and ASD patients. a, Individualized deviation scores of MDD (N = 622) and ASD (N = 653) patients compared to the median of health controls. For each metric, the significance of the median differences between each disease group and health controls was assessed using the Mann-Whitney U test. P values were adjusted for multiple comparisons using the Benjamini-Hochberg false discovery rate (FDR) correction across all possible pairwise tests. The violin-box-hybrid plots from left to right represent the patient's deviation score distributions for whole-brain functional connectivity (FC), individualized atlas similarity, and individualized system segregation, respectively, wherein the median of the control group is depicted as a horizontal blue dotted line. The right panel illustrates case-control group differences in deviation scores of regional FC. Vertices that passed FDR correction were visualized as Z values, with higher absolute Z values indicating more significant median differences (positive Z values signifying a positive deviation). **b**, Percentage of patients with extreme deviations. Subplots from left to right display the percentage of subjects with extreme deviations in MDD and ASD populations for whole-brain FC, individualized atlas similarity, individualized system segregation, and regional FC. Red represents extreme positive deviations, while blue indicates extreme negative deviations. All brain maps were mapped to the HCP fs_LR_32k surface for visualization. VIS, visual; SM, somatomotor; DA, dorsal attention; VA, ventral attention; LIM, limbic; FP, frontoparietal; DM, default mode.

Compared to the healthy control (HC) group, patients with MDD showed significant differences in deviation scores for global mean and variance of functional connectome ($p < 0.001$, false discovery rate (FDR) corrected, Fig. 5a). MDD patients exhibited significant differences in deviation scores across 17 of 18 connectomic metrics at the whole-brain and system level, ($p < 0.001$, FDR corrected), and ASD patients exhibited significant differences in 10 metrics ($p < 0.001$, FDR corrected). Notably, all these significant deviations were negative, suggesting a

disruption in the system's functional organization in both diseases. At the regional level, MDD patients had significantly larger deviations than HCs in 44.4% vertexes ($p < 0.05$, FDR corrected), with positive deviations (1.6% vertexes) in the bilateral supramarginal gyrus cortex and negative deviations (42.8% vertexes) mainly in the visual, sensorimotor, precuneus, and superior parietal cortex. For ASD patients, 15.4% of vertexes had significantly larger deviations than in HCs ($p < 0.05$, FDR corrected), with positive deviations (7.0% vertexes) in the prefrontal and precuneus cortex and negative deviations (8.4% vertexes) mainly in the sensorimotor cortex.

To access the interindividual heterogeneity, we calculated the overall negative and positive extreme deviations across all metrics (at the whole-brain, system, and regional levels) in each participant. For MDD patients, 98.9% showed at least one negative extreme deviation, and 52.7% showed at least one positive extreme deviation (Supplementary Fig. 8). For ASD patients, the ratios were 98.3% and 35.1%. To access inter-metric heterogeneity, we calculated the proportion of extreme deviations across all participants in each metric. In most whole-brain and system-level connectomic metrics, the proportion of subjects with extreme negative deviations exceeded those with extreme positive deviations (Fig. 5b, left panel). For the functional metrics at the regional level (Fig. 5b, right panel), the extreme positive deviations in MDD patients were mostly located in the bilateral prefrontal cortex, angular gyrus, and temporal cortex, and extreme negative deviations were widespread over the whole brain, especially in the precuneus and temporal cortex. For ASD patients, the extreme positive deviations were in the precuneus, prefrontal, and angular gyrus cortex, and extreme negative deviations were also widespread over the whole brain.

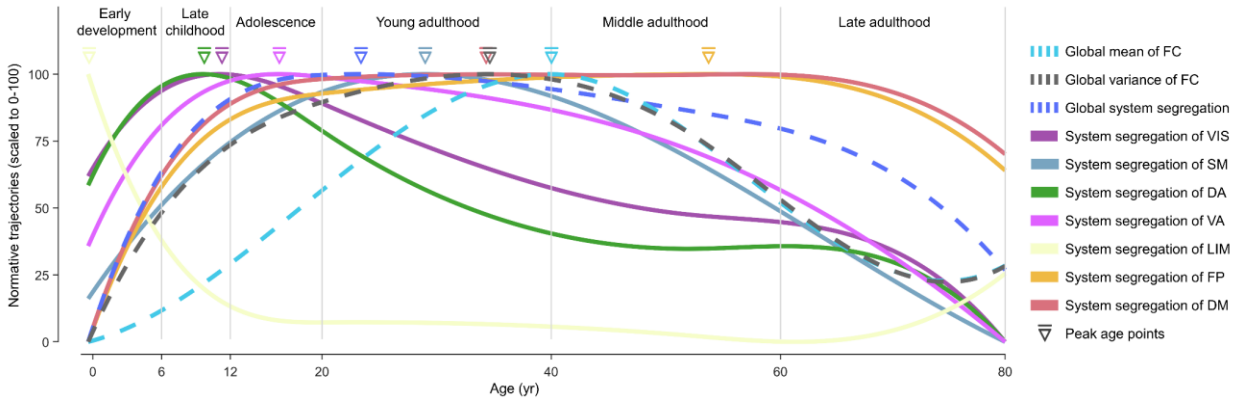

Fig. 6 | A graphical representation illustrating the life-course normative trajectories of the functional connectome at the global and system levels. The growth trajectories (50% centile) estimated by GAMLSS for each metric were normalized to a 0-100 scale. Dashed lines represent trajectories for the global mean of FC, global variance of FC, and global system segregation; while solid lines depict those for system segregation of each subnetwork. Triangles depict the peak points for each connectomic metric. FC, functional connectome; VIS, visual; SM, somatomotor; DA, dorsal attention; VA, ventral attention; LIM, limbic; FP, frontoparietal; DM, default mode. yr, year.

Discussion

In this study, we assembled, to our knowledge, the most extensive multimodal imaging dataset to date, spanning the human lifespan, to comprehensively chart the growth trajectories of the functional connectome. Through systematic analysis at the whole-brain, system, and regional levels, we mapped the multiscale non-linear trajectories of functional organization and unveiled previously unidentified, key growth milestones from a network perspective (Fig. 6). To provide a lifespan characterization of large-scale functional systems, we established age-specific atlases spanning 32 postmenstrual weeks to 80 years of age, serving as a foundational resource for future research on brain network development and aging. By leveraging two large disease datasets, ABIDE for Autism Spectrum Disorder (N=653) and DIDA-MDD for Major Depressive Disorder (N=622), we explored the utility of the connectome-based normative model in capturing individual heterogeneity within these clinical populations, thereby underscoring its potential for advancing our understanding of neuropsychiatric disorders.

At the whole-brain level, we observed continuous non-linear changes in the global mean and variance in functional connectivity across the life cycle, reaching peaks in the fourth decade with a relatively narrow CI. Likewise, the developmental trajectory in global brain structure shows a pattern of increase followed by decline, albeit peaking earlier [18]. These functional and anatomical findings collectively suggest that the human brain remains in a state of dynamic adaptation throughout its lifespan. At the system level, one intriguing observation is that, relative to other networks, the DM and FP networks undergo more rapid development of system segregation during infancy, childhood, and adolescence, reach their peaks later, and exhibit a more precipitous decline during aging. The accelerated early development of these networks can be attributed to their initially less organized functional architecture in utero [49, 77] and the subsequent imperative for rapid postnatal development to support the emergence and evolution of advanced cognitive functions [8, 78, 79]. Moreover, the heightened susceptibility of these networks to accelerated decline in the aging phase may be compounded by their increased sensitivity to environmental, genetic, and lifestyle factors, as well as neurodegenerative agents such as amyloid-β and tau [80-83]. At the regional level, our results validated and extended the replicable findings reported by Luo and colleagues [31], who observed an increase in FCS in primary regions and a decrease in higher-order areas from childhood to adolescence using four independent datasets. Furthermore, the life-cycle growth trajectory of regional FCS is constrained by its position along the S-A axis, underscoring the role of the S-A axis as a key organizational principle that influences cortical development and aging [62].

Emerging evidence increasingly implicates aberrant interregional brain communication and global network dysfunction as critical factors in the pathogenesis of diverse neuropsychiatric disorders [13, 15, 16]. After constructing lifespan growth curves, we focused on characterizing the degree to which individual functional metrics deviated from established norms of the population. This provides preliminary insights into the clinical utility of our functional normative model. By employing age- and sex-normalized metrics, we revealed individual heterogeneity in functional brain deviations at the whole-brain, system, and regional levels in two clinically relevant populations: ASD and MDD. Our results elucidated patterns of deviations across different metrics for these two disorders. For instance, regions displaying extreme positive deviations in FCS were broadly consistent between ASD and MDD patients, whereas those showing extreme negative deviations differed. Across both whole-brain and system levels, individuals with

extreme negative deviations were generally more prevalent than those with extreme positive deviations in both conditions. Further exploration into the underlying causes of these extreme positive and negative functional deviations could yield valuable insights into the commonalities and distinctions between these disparate clinical disorders [73]. Note that, substantial work remains to translate growth charts and their derived heterogeneity metrics effectively into clinical utility [18, 84, 85]. For example, using the individual deviation scores across multiscale functional metrics, we could identify biological subtypes with shared connectome patterns. Assessing whether extreme deviations in functional metrics are associated with symptom severity or cognition is crucial. Therapeutically, incorporating individual functional deviations along with finely stratified subtypes might improve the efficacy of interventions through the connectome-guided transcranial magnetic stimulation [86]. Finally, future studies could be conducted by encompassing more disease cohorts with large sample sizes to enable transdiagnostic comparisons among disorders. In summary, the integration of the connectomic framework with normative growth trajectories offers an unprecedented opportunity for the investigation of brain network dysfunction in clinical populations.

In addition, an intriguing avenue to explore in future research is the interaction between brain networks' life-span trajectories under different modalities—specifically, how various connectivity metrics coevolve throughout the lifespan and whether similar or variable temporal key points exist within these trajectories. It is necessary to determine whether structural connectome milestones precede those of functional connectome, thereby providing an anatomical scaffold for the dynamic maturation of functional communication. Moreover, uncovering the critical physiological factors that shape life-course growth trajectories is complex but essential. Recent findings indicated that the population-based life-cycle trajectories of cortical thickness align with the patterns of molecular and cellular organizations, with varying degrees of biological explanations at different life stages [87]. A genome-wide association meta-analysis performed by Liu et al. [88] identified common genetic variants that influence the rates of change in cortical morphology growth or atrophy across the lifespan. These insights emphasize the importance of adopting a multidimensional approach—encompassing anatomy, genetics, molecular, and metabolism—to decode the intricate factors governing the typical and atypical changes in the human brain connectome.

Several challenges warrant further consideration. First, in the current study, the data used for delineating lifespan growth trajectories were aggregated from existing neuroimaging datasets, which are disproportionately derived from European, North American, Asian, and Australian populations. Inevitably, this geographic bias was also found in other neuroimaging normative references or big data studies, such as those involving cortical morphology growth charts [18] and genome-wide association studies of brain structure across the lifespan [88]. Future efforts should incorporate more neuroimaging cohort studies designed to achieve a balanced representation of diverse ethnic populations [89]. Additionally, it is critical to consider the diversity of environmental factors such as socio-economic status, education level, industrialization, and regional culture, in posing potential challenges for the application of developmental trajectories. Second, similar to the limitations outlined by Bethlehem et al. [18], we also encountered challenges related to uneven age distribution in the neuroimaging sample, particularly with underrepresentation in the infant and middle-aged (30-40 years) populations. Functional changes are dramatic in the utero brain, but the scarcity of available fetal fMRI data limits our understanding of this critical period. Future research should augment our current models with functional neurodevelopment data from

fetal stages. In the present study, we aggregated the largest data sample of task-free fMRI to date, with 33,809 brain scans from 32,328 individuals across the lifespan. Nonetheless, the majority of the data is still cross-sectional, which could in part underestimate age-related actual changes in functional connectome observed in longitudinal measurements [90]. Therefore, the integration of more densely collected longitudinal data is imperative for a precise characterization of life-cycle developmental trajectories. Finally, we anticipate that the connectome-based growth charts established herein will serve as a dynamic resource. We will continue to update the lifespan growth model as more high-quality, multimodal connectome datasets become available.

Methods

Datasets and participants

To curve the normative growth of the functional connectome in the human brain, we sought to aggregate the available multi-site neuroimaging scans, each featuring both 3T structural and task-free fMRI data. For subjects with multiple test-retest scans, only the first session was included. In cases where longitudinal scans were available, all scans were incorporated into the analysis. In total, our dataset comprised 45,525 scans (N = 43,377) from individuals ranging in age from 32 postmenstrual weeks to 80 years, and across 148 sites in 24 datasets. Detailed scanning parameters and demographic information for each dataset are provided in Supplementary Table 1. Written informed consent of participants or their guardians was approved by the local ethics committees for each dataset.

Image quality control process

The implementation of a rigorous and standardized procedure for quality control is essential to guarantee the authenticity of neuroimaging data, thus enhancing the credibility of growth curves. Previous research has shown that inadequate quality control of MRI scans can diminish the advantages of large sample size in detecting meaningful associations [91]. In this study, we adopted a comprehensive four-step data quality control framework, combining automated assessment tools and expert manual review, to assess both structural and functional images across all 45,525 scans (Supplementary Fig. 1). This strict framework effectively identified imaging artifacts or errors, thereby ensuring the accuracy and reliability of our neuroimaging data.

Step 1: Quality control for raw images. First, we conducted preliminary quality control to filter out low-quality scans with problematic acquisitions. For several publicly available datasets (dHCP, HCP-Development, HCP-Aging, HCP-Young Adult, and ABCD) that provide imaging quality information, we performed initial quality control according to their recommended inclusion criteria. For BCP dataset, two neuroradiologists experienced in pediatric MRI visually examined each scan. For other datasets, we employed automated quality assessments using the MRI Quality Control (MRIQC) tools [92], which extracted no-reference quality metrics for each structural (T1w and T2w) and fMRI image. In each dataset, structural images were excluded if they were marked as outliers (over 1.5x the interquartile range (IQR) in the adverse direction) in at least three of the following quality metrics: entropy-focus criterion (EFC), foreground-background energy ratio (FBER), coefficient of joint variation (CJV), contrast-to-noise ratio (CNR), signal-to-noise ratio (SNR), and Dietrich's SNR (SNRd). Similarly, functional images were excluded if they were marked as outliers in three or more of the following quality metrics: AFNI's outlier ratio (AOR), AFNI's quality index (AQI), DVARS_std, DVARS_vstd,

SNR, temporal signal-to-noise ratio (tSNR). This step led to the exclusion of 818 structural and 941 functional images.

Step 2: Whether to pass the whole processing pipeline. After the initial quality control step, the images were subjected to the preprocessing and postprocessing pipelines. A detailed description of the data processing pipelines is provided in the following section. Any scan that could not undergo the entire data processing pipeline was excluded, resulting in the removal of 2,859 structural and 2,914 functional images.

Step 3: Surface quality control and head motion control. For structural images, we utilized the Euler number to assess the quality of the reconstructed cortical surface. The Euler number is a mathematical concept that summarizes the topological complexity of a surface, which can be calculated as 2-2n, where n represents the number of defects such as holes or handles. A high Euler number represents a surface with fewer defects, indicating high-quality cortical surface reconstruction. The Euler number is a reliable and quantitative measure and can be used to identify unusable images [18, 91, 93]. Similarly, the images with an Euler number magnitude less than 1.5x the IQR in the adverse direction from the study-specific distribution (Q1–1.5*IQR) were identified as outliers and excluded. For functional images, scans with large head motion (mean framewise displacement (FD) > 0.5 mm, or frames with FD over 0.5 mm > 20%) were excluded, along with scans having fewer than 100 final time points or the ratio of final time points to original time points < 90%. In total, we excluded 2,045 structural images and 3,493 functional images.

Step 4: Visual double-check. Finally, we put together a team of four experts to visually double-check the quality of the images. Specifically, we excluded structural images that failed due to issue segmentation, surface reconstruction, surface registration, or myelination distribution and excluded functional images that failed due to function-to-structure registration or volume-to-surface mapping. In this step, 629 structural images and 1,139 functional images were excluded. Ultimately, only scans that successfully passed quality control for both functional and structural images were retained.

Applying the above rigorous criteria led to the exclusion of 10,441 scans in 9774 subjects. The final sample comprised 35,084 scans with high-quality functional and structural images across 119 sites, including 33,809 scans (N = 32,328) from HCs, 653 scans (N = 653) from individuals diagnosed with ASD, and 622 scans (N = 622) from individuals diagnosed with MDD.

Data processing pipeline

(i) Structural data preprocessing. While we sought to use a consistent structural preprocessing pipeline across all datasets to minimize the impact of varying methods, the considerable changes in the human brain across the lifespan made this challenging. This was particularly evident in the perinatal and infancy periods, where the anatomical characteristics differ markedly from those in adults. For instance, in six-month-old infants, the contrast between gray and white matter is extremely subtle, and at approximately six months of age, there is a contrast inversion in the gray and white matter. These factors greatly complicate brain tissue segmentation during this period [94, 95]. Due to the lack of a preprocessing pipeline suitable for all life-course stages, it is necessary to seek appropriate methods for datasets in early developmental stages while ensuring the uniformity of the pipelines in other datasets.

For individuals aged three years and older, we utilized the publicly available, containerized HCP

structural preprocessing pipelines (v4.4.0-rc-MOD-e7a6af9) [96], which have been standardized through the QuNex platform (v0.93.2) [97]. In brief, this pipeline involves three stages: (1) The PreFreeSurfer stage focused on the normalization of anatomical MRI data, involving a sequence of preprocessing steps that include brain extraction, denoising, and bias field correction on anatomical T1- and T2w MRI data (if T2w data were available). (2) The FreeSurfer stage entailed the creation of cortical surfaces from the normalized anatomical data, involving anatomical segmentation; the construction of pial, white, and mid-thickness surfaces; and surface registration to the standard atlas. (3) The PostFreeSurfer stage converted the outputs from the previous steps into HCP format (CIFTI). The volumes were transformed to a standard template space using non-linear registration, while the surfaces were mapped to the standard fs_LR_32k space through spherical registration and surface downsampling. To mitigate the computational burden in processing the extensive ABCD dataset, we opted to utilize the community-shared, preprocessed data released through the ABCD-BIDS Community Collection [98] (ABCD collection 3165; https://github.com/ABCD-STUDY/nda-abcd-collection-3165). The neuroimaging data underwent preprocessing using the ABCD-HCP pipeline, a variant of the HCP pipeline adapted to better suit the ABCD dataset. The modifications in the ABCD-HCP structural pipeline include volume registration algorithms and bias field correction methods. Further details regarding these adjustments can be found in the online document (https://collection3165.readthedocs.io/en/stable/pipelines/).

For participants within the postmenstrual age range of 32 to 44 weeks from the dHCP study, we applied the officially recommended dHCP structural pipelines [99], which have been specifically developed to address the substantial differences between neonatal and adult MRI data. This HCP-style pipeline comprised the following stages: (1) bias correction and brain extraction performed on the motion-corrected, reconstructed T2-weighted images; (2) tissue segmentation; (3) cortical reconstruction of the white matter surface; (4) surface topology correction; (5) generation of pial and mid-thickness surfaces; (6) generation of inflated surfaces derived from the white matter surface through an expansion-based smoothing process; (7) projection of the inflated surface onto a sphere for surface registration. Likewise, for participants aged 0-3 years from the BCP study, we employed the officially recommended iBEAT V2.0 pipelines [100]. This pipeline, optimized for early-age neuroimaging data preprocessing based on advanced algorithms, has shown superior performance in tissue segmentation and cortical reconstruction for BCP datasets compared to alternative approaches. The stages of this pipeline mainly included (1) inhomogeneity correction of T1w/T2w images; (2) skull stripping and cerebellum removal (for subjects with incomplete cerebellum removal, frame-by-frame manual corrections were conducted); (3) tissue segmentation; (4) cortical surface reconstruction; (5) topological correction of the white matter surface; (6) final reconstruction of inner and outer cortical surfaces.

Based on the individual cortical surface obtained from the dHCP and iBEAT V2.0 structural pipelines, we employed a three-step registration method to align with the fs_LR_32k standard space of adults (Supplementary Fig. 2). For participants aged 32 to 44 postmenstrual weeks, we implemented the following steps: (1) individual surfaces were registered to their respective postmenstrual week templates [101]; (2) templates for 32-39 postmenstrual weeks and 41-44 postmenstrual weeks were registered to the 40-week template; and (3) the 40-week template was subsequently registered to the fs_LR_32k surface template. For participants aged 0-36 months, the steps involved were as follows: (1) individual surfaces were registered to their corresponding monthly age templates [102]; (2) all monthly templates were registered to the 12-month template;

and (3) the 12-month template was then registered to the fs_LR_32k surface template.

(ii) Functional data preprocessing in volumetric space. For individuals aged three years and older, we employed the HCP functional preprocessing pipelines [96]. The fMRIVolume stage consisted of the following steps. (1) Slice timing correction: This step was applied only for single-band acquisitions, as multiband acquisitions did not necessitate slice timing correction. (2) Motion correction: EPI images were aligned to the single-band reference image using 6 DOF FLIRT registration. In cases where the single-band imaging data were unavailable, the first frame of the fMRI data served as the reference. Motion parameters, including translations, rotations, and their derivatives were recorded. The demeaned and linearly detrended parameter is also provided for nuisance regression analysis. (3) EPI distortion correction: Geometric distortion correction was conducted using the opposite-phase encoding spin-echo images (if LR-RL or AP-PA encoded acquisitions were available) or through the regular (gradient-echo) fieldmap images (if fieldmap acquisitions were available). When neither image was available, this step was omitted. (4) Anatomical registration: The fMRI images were registered to the T1w image utilizing 6 DOF FLIRT with the boundary-based registration (BBR). (5) Intensity normalization: The fMRI data, masked by the final brain mask from the PostFreeSurfer structural pipeline, were normalized to a 4D whole-brain mean of 10,000.

For participants within the postmenstrual age range of 32 to 44 weeks from the dHCP study, we applied the dHCP functional pipelines [103]. Building upon the foundation of the HCP pipeline and the FSL FEAT pipeline, this pipeline was tailored to address the unique challenges inherent to neonatal fMRI data. The key components of the pipeline encompassed the following: (1) fieldmap preprocessing, which entails estimating the susceptibility distortion field based on the opposite-phase encoding spin-echo images and subsequently aligning this field with the functional data; (2) registration, which involves BBR of the fieldmap magnitude to the T2w image, BBR of the single-band reference image to the T2w image with incorporation of field map-based distortion correction, and 6 DOF FLIRT registration of the first volume of the functional multiband EPI to the single-band reference image; and (3) susceptibility and motion correction, which includes performing slice-to-volume motion correction and motion-by-susceptibility distortion correction, along with estimating motion nuisance regressors. Through these steps, we obtained distortion-corrected and motion-corrected 4D multiband EPI images in the T2w native volumetric space. For participants aged 0-3 years from the BCP study, we implemented several steps to obtain preprocessed volumetric fMRI data. (1) Motion correction: functional images were aligned to the single-band reference image using 6 DOF FLIRT registration. When a single-band reference was not available, we used the mean functional images (with all frames aligned to the first frame) as the reference. (2) Distortion correction: we performed distortion correction based on the opposite-phase encoding (AP-PA) spin-echo images. This step was only conducted for participants with available acquisitions. (3) EPI to anatomical registration: we aligned the reference image with the anatomical image (T1w or T2w) using 6 DOF FLIRT registration.

(iii) Functional data preprocessing in surface space. In the fMRISurface stage of the HCP functional pipeline, the aim was to project the volume time series onto the standard CIFTI grayordinates space, which incorporates surface-based cortical data along with volume-based subcortical and cerebellar data. For the data from the dHCP and BCP studies, to achieve an accurate representation of cortical BOLD signals on the surface, we followed the same steps in the HCP preprocessing pipeline. Specifically, the fMRI volumetric data in the cortical cortex

were separated into left and right hemispheres and mapped onto each participant's mid-thickness surfaces using a partial-volume weighted, ribbon-constrained volume-to-surface mapping algorithm [96]. Subsequently, employing each participant's surface registration transformations from the structural preprocessing stage, the time courses were transferred from the individual's native space to the fs_LR_32k standard space.

(iv) Functional data postprocessing. For ABCD dataset, the ABCD-HCP functional pipeline used the DCANBOLDProcessing software (https://collection3165.readthedocs.io/en/stable/pipelines/) to reduce spurious variance unlikely to reflect neuronal activity. For other datasets, the preprocessed fMRI data were postprocessed using SPM12 (v6470) and GRETNA (v2.0.0) with a uniform pipeline. Specifically, we first conducted the following steps on the time series for each vertex in fs_LR_32k space (a total of 59,412 vertices): linear trend removal, nuisance signal (24 head motion parameters, white matter signal, cerebrospinal fluid signal, and global signal) regression, and temporal bandpass filtering (0.01–0.08 Hz). We implemented scrubbing to mitigate the effects of head motion; volumes with FD greater than 0.5 mm and their adjacent volumes (1 prior and 2 subsequent) were replaced with linearly interpolated data. Then, surface-based smoothing was applied using a 6-mm full-width at half-maximum (FWHM) kernel. Ultimately, the data were resampled to a mesh of 2,562 vertices (corresponding to the fsaverage4 standard space) for each hemisphere using the HCP Workbench metric-resample command. Due to the inclusion of the medial wall, the combined number of vertices exhibiting BOLD signals on both left and right hemisphere surfaces amounted to 4,661.

Construction of the age-specific functional atlas over the lifespan

(i) Population-level age-specific atlas construction. To enhance the precise mapping of individual-specific functional networks across the life course, we first developed a Gaussian-weighted iterative age-specific group atlas (GIAGA) generation approach (Supplementary Fig. 3) to establish a set of age-specific population-level functional atlases to guide individual iteration (Fig. 2a, Supplementary Fig. 4). Considering the dramatic functional changes during early development [53], we prioritized creating a higher number of age-specific atlas for these stages compared to later life stages. Specifically, we partitioned all individual scans into 26 distinct age subgroups spanning from 32 postmenstrual weeks to 80 years of age, and constructed a specific functional atlas for each subgroup. We established 9 atlases for the perinatal to early infancy stages, including 4 for perinatal development (34-week, 36-week, 38-week, and 40-week (0-year) atlases) and 5 for the first year of life (1-month, 3-month, 6-month, 9-month, and 12-month atlases). We developed 2 atlases for toddlers (18-month and 24-month atlases), 9 atlases for children to late adolescents (4-year, 6-year, 8-year, 10-year, 12-year, 14-year, 16-year, 18-year, and 20-year atlases), and 6 atlases for adults and elderly persons (30-year, 40-year, 50-year, 60-year, 70-year, and 80-year atlases). For the construction of the functional atlas for each age subgroup, we randomly selected individual scans from 300 participants. If the sample size was less than 300, we included all scans after quality control. Detailed information on the age range, number of participants, and sex ratio for each atlas is shown in Supplementary Table 2.

In recent studies of brain functional organization, Yeo's 7- and 17-networks atlas [54] have been widely adopted to map the cortical functional systems [104]. By incorporating hand sensorimotor areas based on activations in a hand motor task [105], Wang and colleagues extended this classical functional parcellation, resulting in an 18-network atlas [55]. In line with previous studies [43, 56, 57], we utilized this updated classical 18-network map as the initial atlas for constructing age-specific

functional atlases. The detailed construction process for a given age subgroup (e.g., 17-19 years) was as follows. First, to enhance the dataset for this age subgroup, we incorporated the latter half of the previous subgroup's scans and the earlier half of the subsequent subgroup's scans. We then employed the individualized parcellation iteration algorithm proposed by Wang and colleagues [55] to map the 18-network atlas to each participant, generating the initial individualized functional parcellations (Step 1 in Supplementary Fig. 3a). Subsequently, we proposed the GIAGA approach. Centering around the core age (i.e., 18 years) of this given group, we generated a Gaussian probability distribution $N(\mu, \sigma^2)$ with mean $\mu = 0$ and standard deviation $\sigma = 1$ and assigned weights to each participant based on their age's position in this Gaussian distribution. The weight quantified the participant's contribution to the population-level atlas construction, with proximity to the core age resulting in a greater contribution. For each vertex, we calculated the across-participant cumulative probability belonging to each network, and assigned vertex labels to the network with the highest cumulative probability, resulting in an initial age-specific population-level atlas (Step 2 in Supplementary Fig. 3a). Finally, we iteratively repeated Steps 1 and 2 until the overlap between the current and previous atlases exceeded 95% or the total number of iterations surpassed 10, indicating convergence (Step 3 in Supplementary Fig. 3a).

(ii) Individualized atlas construction. For a given participant, we used the same iterative parcellation method mentioned above to generate an individualized functional parcellation based on the corresponding population-level atlas specific to the participant's subgroup (Supplementary Fig. 3b, adjusted from [55]). Briefly, the influence of the population-level atlas on the individual brain varied among subjects and across brain regions; therefore, this method made flexible modifications during the individualized atlas construction based on the distribution of intersubject variability in the functional connectome and the tSNR of the functional BOLD signals. Throughout the iterations, the weighting of population-based information progressively decreased, allowing the concluding individualized map to be completely driven by the individual-level BOLD data. More information on this iterative functional parcellation approach can be found in the study by Wang and colleagues [55].

Notably, considering the potential variance for distinct interindividual variability patterns and tSNR distributions across different age subgroups, we generated an interindividual variability map and a tSNR map for each age subgroup. This was done to enhance the precise mapping of both the individualized and population-level atlases. We divided the time series data of each participant within each age subgroup into two halves, and for each half, we computed a vertex-by-vertex functional connectome matrix. This allowed us to obtain the intersubject variability and intrasubject variability within the subgroup. By regressing the intrasubject variability from the intersubject variability, we obtained a "purified" measure of intersubject variability in the functional connectome [106, 107].

(iii) Constructing reference atlas used for comparison. To mitigate the potential bias introduced by specifying a reference atlas for 'mature age', we opted for a data-driven approach to construct the reference atlas. Atlas similarity was assessed using the overlap index, which quantifies the proportion of vertices with matching labels between two atlases. For instance, if two atlases have 4,000 vertices with identical labels out of a total of 4,661 vertices, the overlap index would be 4,000/4,661 = 85.8%. We computed the overlap index between each pair of the 26 atlases, resulting in a 26×26 similarity matrix. Hierarchical clustering was applied to this matrix, as illustrated in Supplementary Fig. 5a. We selected a highly congruent subset of atlases, including

the 18-, 20-, 30-, 40-, 50-, 60-, and 70-year atlases. For each vertex, we assigned the label as the system that exhibited the highest occurrence probability across these selected atlases, thereby generating the final reference atlas (Supplementary Fig. 5b).

Individualized metrics of the functional connectome

For each pair of vertices among the 4,661 vertices in fsaverage4 space, we computed the Pearson correlation coefficient to characterize the region-by-region functional connectivity, resulting in a 4,661×4,661 functional connectome matrix for each participant. Any negative functional connectivity strengths were reset to zero. For each participant, the overall mean of functional connectivity across the whole brain was defined as the average of all 4,661×4,661 connections (edges), and the variance in functional connectivity was defined as the standard deviation of all 4,661×4,661 connections. The FCS of a specific vertex was quantified as the average connections with all other vertices. For a given brain system, an individual's within-system functional connectivity FC_w was defined as the average connection strength among all vertices within this personalized system. Conversely, the individual's between-system connectivity FC_b was represented by the average strength of connections between this system and all other systems. The system segregation [59] was determined by calculating the difference between FC_w and FC_b, normalized by FC_w, as described in the following formula:

$$\text{System segregation} = \frac{FC_w - FC_b}{FC_w}$$

Similarly, whole-brain system segregation was defined as the difference between whole-brain mean within-system connectivity and whole-brain mean between-system connectivity, normalized by whole-brain mean within-system connectivity.

The individualized whole-brain atlas similarity was defined by the overlap index with the reference atlas. If there were 4,661 vertices with the same label in two atlases, the overlap index was 4,661/4,661 = 1. The similarity of an individualized system was quantified using the Dice coefficient relative to its corresponding system in the reference atlas.

Multisite data harmonization

In studies that involve multisite datasets, it is critical to account for and remove site-specific effects to ensure that measurements across different sites are directly comparable. The ComBat method [108] and its variants [109, 110] are increasingly used for harmonizing neuroimaging data across multiple sites. In the present study, we employed ComBat with generalized additive model (GAM) for harmonization. We included age, sex, and disease type as the biological variables that need to be protected, with age was set as a smooth term[109]. This approach allowed us to remove site-specific differences in individual functional connectome metrics, while retaining the ability to conduct downstream non-linear modeling analyses.

Modeling normative trajectories across the lifespan

To estimate the normative age-dependent curves for various metrics of the brain functional connectome in healthy individuals combined across cohorts, we implemented the GAMLSS [37, 38] using the *gamlss* package (version 5.4-3) in R 4.2.0. We established the GAMLSS procedure with two steps: the identification of the optimal data distribution, followed by the determination of the best-fitting parameters for each functional connectome metric. Utilizing these metric-specific GAMLSS models, we obtained non-linear normative trajectories, as well as their first

derivatives. Moreover, we uncovered sex-stratified developmental patterns. The goodness of model fitting is endorsed by model convergence and visualized by traditional Q-Q (quantile-quantile) plots and detrended transformed Owen's plots. The reliability and robustness of the lifespan growth curves were assessed through bootstrap resampling analysis and leave-one-study-out analysis. Leveraging these population-level normative trajectories, we established benchmarks for each subject using individualized deviation scores.

(i) Model data distributions. While the World Health Organization provides guidelines for anthropometric growth chart modeling (such as head circumference, height, and weight) with the Box-Cox t-distribution as a starting point [37], we recognized that the trajectories of brain neuroimaging metrics might not necessarily adhere to the same underlying distributions. For instance, Bethlehem et al. reported that the generalized gamma distribution offered the best fit for brain tissue volumes [18]. Consequently, we evaluated all continuous distribution families (n=51) for model fitting. To discern the optimal distribution, we fitted GAMLSS with different distributions to four representative whole-brain functional metrics (global mean of functional connectivity, global variance in functional connectivity, whole-brain atlas similarity, and whole-brain system segregation) and assessed model convergence. We used the Bayesian Information Criterion (BIC) to compare model fits among the converged models, with a lower BIC indicating a better fit. As depicted in Supplementary Fig. 9, the Johnson's Su (JSU) distribution consistently provided the best fit across all evaluated models.

(ii) GAMLSS framework. We constructed the GAMLSS procedure with the functional connectome metric as the dependent variable, age as a smooth term (using the B-spline basis function), and sex and in-scanner head motion (HM) as other fixed effects. The JSU distribution, which has four parameters: median (μ), coefficient of variation (σ), skewness (ν), and kurtosis (τ), was chosen to accommodate the data distribution. Each functional connectome metric, denoted with y, was modeled as:

$$y = JSU(\mu, \sigma, \nu, \tau),$$
$$\mu = f_{\mu}^{1}(age) + f_{\mu}^{2}(sex) + f_{\mu}^{3}(HM),$$
$$\sigma = f_{\sigma}^{1}(age) + f_{\sigma}^{2}(sex) + f_{\sigma}^{3}(HM),$$
$$\nu = \beta_{\nu},$$
$$\tau = \beta_{\tau}.$$

Considering the developmental complexity throughout the life cycle, we sought to capture the underlying age-related trends by exploring a range of model specifications. We fitted ten distinct GAMLSS models with different configurations of degrees of freedom (df = 3-6) for the B-spline basis functions in the location (μ) and scale (σ) parameters. Following the practice of previous studies [18, 75], only an intercept term was included for the ν or τ parameters. For model estimation, we used the default convergence criterion of log-likelihood = 0.001 between model iterations and set the maximal iteration cycles as 100. Finally, the optimal model of a given functional metric was selected based on the lowest BIC value among all convergent models. Supplementary Fig. 10 shows the BIC of model selection for the representative whole-brain functional metrics.

(iii) Goodness of model fit. On the one hand, model convergence after iterative fitting can be

used as an indicator of the goodness of model fit. In our study, we observed no instances of nonconvergence in the GAMLSS models for all metrics, including those employed in sensitivity analyses. Furthermore, we checked the normalized quantile residuals of our normative model to evaluate the goodness of fit by utilizing two diagnostic methods. First, we visually inspected four plots related to residuals. As shown in Supplementary Fig. 11, the residuals against the fitted values of μ and the index were evenly distributed around the horizontal line at 0. Moreover, the kernel density estimation of the residuals displayed an approximate normal distribution, and the normal quantile-quantile (Q-Q) plots exhibited an approximately linear trend with an intercept of 0 and a slope of 1. Second, we used the detrended transformed Owen's plots of the fitted normalized quantile residuals to evaluate the performance of the models. The function uses Owen's method to construct a nonparametric confidence interval for the true distribution. As shown in the resulting plots (Supplementary Fig. 12), the zero horizontal line was within the confidence intervals, suggesting that the residuals followed a normal distribution. Taken together, these results showed that our model fits the sample data appropriately.

(iv) Sensitivity analyses of GAMLSS. To validate the reliability and robustness of our life-course developmental trajectory model, we first performed a series of leave-one-study-out analyses. Specifically, we iteratively excluded the dataset from a single study (e.g., the ABCD study) from primary studies, refitted the GAMLSS model, evaluated all model parameters, and then extracted developmental trajectories. We then compared these alternative trajectories to those derived from the full dataset for the whole-brain functional metrics. Our results showed remarkable consistency, with a very high correlation between the trajectories derived from the primary full dataset and those from the subsets (all $r > 0.98$), even when large datasets such as ABCD and UKB were excluded (Supplementary Fig. 13).

To further assess the reliability of lifespan trajectories and obtain their confidence intervals, we performed bootstrap resampling analysis. Specifically, we conducted 1000 bootstrap iterations with replacement sampling. To ensure that the bootstrap replicates preserved the original studies' age and sex proportionality, we segmented the lifespan (from 32 weeks to 80 years) into 10 equal intervals and then conducted stratified sampling based on both age and sex. For each functional metric, we refitted 1000 trajectories and computed 95% CI for both the 50th centile curve and the developmental inflection points. Supplementary Fig. 14 depicts the CI for the developmental trajectories (50th percentile), underscoring the stability of our lifespan modeling framework.

(v) Sexual difference in lifespan trajectories. In GAMLSS modeling, we included a sex effect as another important feature for establishing lifespan growth of the functional connectome. For the individual1metrics of the functional connectome, the sex-stratified growth curves are shown in Supplementary Fig. 7. These growth curves stratified by sex provide crucial insights into the differential effects of sex on the functional brain connectome across the lifespan.

(iv) Individualized deviation z scores. After establishing normative reference ranges using the GAMLSS model, we calculated individual deviation scores (z scores) for patients with MDD and ASD. Specifically, we first estimated the individual centile scores relative to the normative curves. The deviation z scores were derived by employing the quantile randomized residuals [111], an approach that transforms quantiles of the fitted JSU distribution into standard Gaussian distribution z scores. For healthy subjects, we employed a cross-validation approach to estimate individual deviation scores [73, 75]. During each iteration of the 10-fold cross-validation, we trained a GAMLSS model on the training set, containing 90% of the total sample. We then applied the

fitted model parameters (μ, σ, ν, τ) to the testing set (remaining 10% of the sample) to generate estimated individual centiles. Deviation z scores were subsequently calculated using the quantile randomized residuals approach as well. The normality of the distribution of computed z scores was assessed and endorsed using a two-sided Kolmogorov-Smirnov test, with P values exceeding 0.05 for all functional metrics.

Data availability

The MRI data listed in Supplementary Table 1 are partly available at the Adolescent Brain Cognitive Development Study (https://nda.nih.gov/), the Autism Brain Imaging Data Exchange Initiative (https://fcon_1000.projects.nitrc.org/indi/abide/), the Alzheimer's Disease Neuroimaging Initiative (https://adni.loni.usc.edu/), the Age_ility Project (https://www.nitrc.org/projects/age-ility), the Baby Connectome Project (https://nda.nih.gov/), the Brain Genomics Superstruct Project (https://doi.org/10.7910/DVN/25833), the Calgary Preschool MRI Dataset (https://osf.io/axz5r/), the Cambridge Centre for Ageing and Neuroscience Dataset (https://www.cam-can.org/index.php?content=dataset), the Developing Human Connectome Project (http://www.developingconnectome.org/data-release/second-data-release/), the Human Connectome Project (https://www.humanconnectome.org), the Lifespan Human Connectome Project (https://nda.nih.gov/), the Nathan Kline Institute-Rockland Sample Dataset (https://fcon_1000.projects.nitrc.org/indi/pro/nki.html), the Neuroscience in Psychiatry Network Dataset (https://nspn.org.uk/), the Pixar Dataset (https://openfmri.org/dataset/ds000228/), the Southwest University Adult Lifespan Dataset (http://fcon_1000.projects.nitrc.org/indi/retro/sald.html), the Southwest University Longitudinal Imaging Multimodal Brain Data Repository (http://fcon_1000.projects.nitrc.org/indi/retro/southwestuni_qiu_index.html), and the UK Biobank Brain Imaging Dataset (https://www.ukbiobank.ac.uk/). The dhcpSym surface atlases in aged from 32 to 44 postmenstrual weeks is available at https://brain-development.org/brain-atlases/atlases-from-the-dhcp-project/cortical-surface-template/. The UNC 4D infant cortical surface atlases is available at https://bbm.web.unc.edu/tools/. The fs_LR_32k surface atlas is available at https://balsa.wustl.edu/. The brain charts and lifespan developmental atlases are shared online via GitHub (https://github.com/sunlianglong/BrainChart-FC-Lifespan).

Code availability

The codes for this manuscript are available on GitHub (https://github.com/sunlianglong/BrainChart-FC-Lifespan). Software packages used in this manuscript include MRIQC v0.15.0 (https://github.com/nipreps/mriqc), QuNex v0.93.2 (https://gitlab.qunex.yale.edu/), HCP pipeline v4.4.0-rc-MOD-e7a6af9 (https://github.com/Washington-University/HCPpipelines/releases), ABCD-HCP pipeline v1 (https://github.com/DCAN-Labs/abcd-hcp-pipeline), dHCP structural pipeline v1 (https://github.com/BioMedIA/dhcp-structural-pipeline), dHCP functional pipeline v1 (https://git.fmrib.ox.ac.uk/seanf/dhcp-neonatal-fmri-pipeline), iBEAT pipeline v1.0.0 (https://github.com/iBEAT-V2/iBEAT-V2.0-Docker), MSM v3.0 (https://github.com/ecr05/MSM_HOCR), FreeSurfer v6.0.0 (https://surfer.nmr.mgh.harvard.edu/), FSL v6.0.5 (https://fsl.fmrib.ox.ac.uk/fsl/fslwiki), Connectome Workbench v1.5.0 (https://www.humanconnectome.org/software/connectome-workbench), MATLAB R2018b (https://www.mathworks.com/products/matlab.html), SPM12 toolbox v6470 (https://www.fil.ion.ucl.ac.uk/spm/software/spm12), GRETNA toolbox v2.0.0 (https://www.nitrc.org/projects/gretna), BrainNet Viewer toolbox v 20191031 (https://www.nitrc.org/projects/bnv), cifti-matlab toolbox v2 (https://github.com/Washington-University/cifti-matlab), HFR_ai toolbox v1.0-beta-20181108 (https://github.com/MeilingAva/Homologous-Functional-Regions), System segregation code (https://github.com/mychan24/system-segregation-and-graph-tools), Python v3.8.3 (https://www.python.org), neuroharmonize package v2.1.0

(https://github.com/rpomponio/neuroHarmonize), scikit-learn package v1.1.3 (https://scikit-learn.org). R v4.2.0 (https://www.r-project.org), GAMLSS package v5.4-3 (https://www.gamlss.com/),and ggplot2 package v3.4.2 (https://ggplot2.tidyverse.org/).

Acknowledgments

This work was supported by the National Natural Science Foundation of China (Nos. 82021004, 31830034, 31521063, 31221003, 61431012, 81571062, 81471120, 8143003, 61633018, 81972160, 82172018, 81971690, 81920108019, 82330058, 32130045), Changjiang Scholar Professorship Award (No. T2015027). We are grateful to the Adolescent Brain Cognitive Development (ABCD) Study, the Autism Brain Imaging Data Exchange (ABIDE) Initiative, the Alzheimer's Disease Neuroimaging Initiative (ADNI), the Age_ility Project, the Baby Connectome Project (BCP), the Brain Genomics Superstruct Project (BGSP), the Calgary Preschool MRI Dataset, the Cambridge Centre for Ageing and Neuroscience (Cam-CAN) Dataset, the developing Human Connectome Project (dHCP), the Human Connectome Project (HCP), the Lifespan Human Connectome Project (HCPA & HCPD), the Nathan Kline Institute-Rockland Sample (NKI-RS) Dataset, the Neuroscience in Psychiatry Network (NSPN) Dataset, the Pixar Dataset, the Southwest University Adult Lifespan Dataset (SALD), the Southwest University Longitudinal Imaging Multimodal (SLIM) Brain Data Repository, the UK Biobank (UKB) Brain Imaging Dataset, the Disease Imaging Data Archiving: major depressive disorder (DIDA-MDD) Working Group (PI: Yong He, Lingjiang Li, Jingliang Cheng, Qiyong Gong, Ching-Po Lin, Jiang Qiu, Shijun Qiu, Tianmei Si, Yanqing Tang, Fei Wang, Peng Xie, Xiufeng Xu, and Mingrui Xia), the Multi-center Alzheimer Disease Imaging (MCADI) Consortium (PI: Yong Liu, Xi Zhang, Yuying Zhou, Ying Han, and Qing Wang). We thank the National Center for Protein Sciences at Peking University in Beijing, China, for assistance with MRI data acquisition.

ABCD: data used in the preparation of this article were obtained from the Adolescent Brain Cognitive Development (ABCD) Study (https://abcdstudy.org), held in the NIMH Data Archive (NDA). This is a multisite, longitudinal study designed to recruit more than 10,000 children age 9-10 and follow them over 10 years into early adulthood. The ABCD Study® is supported by the National Institutes of Health and additional federal partners under award numbers U01DA041048, U01DA050989, U01DA051016, U01DA041022, U01DA051018, U01DA051037, U01DA050987, U01DA041174, U01DA041106, U01DA041117, U01DA041028, U01DA041134, U01DA050988, U01DA051039, U01DA041156, U01DA041025, U01DA041120, U01DA051038, U01DA041148, U01DA041093, U01DA041089, U24DA041123, U24DA041147. A full list of supporters is available at https://abcdstudy.org/federal-partners.html. A listing of participating sites and a complete listing of the study investigators can be found at https://abcdstudy.org/consortium_members/. ABCD consortium investigators designed and implemented the study and/or provided data but did not necessarily participate in the analysis or writing of this report. This manuscript reflects the views of the authors and may not reflect the opinions or views of the NIH or ABCD consortium investigators. The ABCD data repository grows and changes over time. The ABCD data used in this report came from https://nda.nih.gov/edit_collection.html?id=3165, shared by the DCAN Labs ABCD-BIDS Community Collection (ABCC) (Collection Investigators: Damien Fair).

ABIDE I: primary support for the work by Adriana Di Martino was provided by the (NIMH K23MH087770) and the Leon Levy Foundation. Primary support for the work by Michael P.

Milham and the INDI team was provided by gifts from Joseph P. Healy and the Stavros Niarchos Foundation to the Child Mind Institute, as well as by an NIMH award to MPM (NIMH R03MH096321).

ABIDE II: primary support for the work by Adriana Di Martino and her team was provided by the National Institute of Mental Health (NIMH 5R21MH107045). Primary support for the work by Michael P. Milham and his team provided by the National Institute of Mental Health (NIMH 5R21MH107045); Nathan S. Kline Institute of Psychiatric Research). Additional Support was provided by gifts from Joseph P. Healey, Phyllis Green and Randolph Cowen to the Child Mind Institute.

ADNI: data used in preparing this article were obtained from the Alzheimer's Disease Neuroimaging Initiative (ADNI) database (adni.loni.usc.edu). As such, many investigators within the ADNI contributed to the design and implementation of ADNI and/or provided data but did not participate in analysis or writing of this report. A complete listing of ADNI investigators may be found at http://adni.loni.usc.edu/wp-content/uploads/how_to_apply/ADNI_Acknowledgement_List.pdf. Data collection and sharing for this project was funded by the Alzheimer's Disease Neuroimaging Initiative (ADNI) (National Institutes of Health Grant U01 AG024904) and DOD ADNI (Department of Defense award number W81XWH-12-2-0012). ADNI is funded by the National Institute on Aging, the National Institute of Biomedical Imaging and Bioengineering, and through generous contributions from the following: AbbVie, Alzheimer's Association; Alzheimer's Drug Discovery Foundation; Araclon Biotech; BioClinica, Inc.; Biogen; Bristol-Myers Squibb Company; CereSpir, Inc.; Cogstate; Eisai Inc.; Elan Pharmaceuticals, Inc.; Eli Lilly and Company; EuroImmun; F. Hoffmann-La Roche Ltd and its affiliated company Genentech, Inc.; Fujirebio; GE Healthcare; IXICO Ltd.;Janssen Alzheimer Immunotherapy Research & Development, LLC.; Johnson & Johnson Pharmaceutical Research & Development LLC.; Lumosity; Lundbeck; Merck & Co., Inc.; Meso Scale Diagnostics, LLC.; NeuroRx Research; Neurotrack Technologies; Novartis Pharmaceuticals Corporation; Pfizer Inc.; Piramal Imaging; Servier; Takeda Pharmaceutical Company; and Transition Therapeutics. The Canadian Institutes of Health Research is providing funds to support ADNI clinical sites in Canada. Private sector contributions are facilitated by the Foundation for the National Institutes of Health (www.fnih.org). The grantee organization is the Northern California Institute for Research and Education, and the study is coordinated by the Alzheimer's Therapeutic Research Institute at the University of Southern California. ADNI data are disseminated by the Laboratory for Neuro Imaging at the University of Southern California.

BCP: data used herein is supported by NIH grant (1U01MH110274) and the efforts of the UNC/UMN Baby Connectome Project Consortium.

dHCP: data were provided by the developing Human Connectome Project, KCL-Imperial-Oxford Consortium funded by the European Research Council under the European Union Seventh Framework Programme (FP/2007-2013) / ERC Grant Agreement no. [319456]. We are grateful to the families who generously supported this trial.

HCP: data were provided by the Human Connectome Project, WU-Minn Consortium (Principal Investigators: David Van Essen and Kamil Ugurbil; 1U54MH091657) funded by the 16 NIH Institutes and Centers which support the NIH Blueprint for Neuroscience Research; and by the

Mc-Donnell Center for Systems Neuroscience at Washington University.

HCP Lifespan: data used in this publication was supported by the National Institute of Mental Health of the National Institutes of Health under Award Number U01MH109589 and by funds provided by the McDonnell Center for Systems Neuroscience at Washington University in St. Louis. The content is solely the responsibility of the authors and does not necessarily represent the official views of the National Institutes of Health.

NKI-RS: Funding for key personnel provided in part by the New York State Office of Mental Health and Research Foundation for Mental Hygiene. Additional project support provided by the NKI Center for Advanced Brain Imaging (CABI), the Brain Research Foundation (Chicago, IL), the Stavros Niarchos Foundation, and NIH grant P50 MH086385-S1.

NSPN: The NSPN study was funded by a Wellcome Trust award to the University of Cambridge and the University College London.

UK Biobank: this research has been conducted using data from UK Biobank (www.ukbiobank.ac.uk). UK Biobank is generously supported by its founding funders the Wellcome Trust and UK Medical Research Council, as well as the Department of Health, Scottish Government, the Northwest Regional Development Agency, British Heart Foundation and Cancer Research UK.

Competing interests

The authors declare that they have no competing interests.

Author contributions

L.L.S. and Y.H. conceptualized the study. Y.H. supervised the project. L.L.S., T.D.Z., X.Y.L., M.R.X. and Y.H. designed the methodology. L.L.S. developed visualizations. Q.L.L., X.H.L., D.N.D., Z.L.Z., Z.L.X. and Z.X.C. provided guidance on data analysis and result interpretation. L.L.S., X.Y.L., Q.W., C.X.P., Q.Y., Q.L.L., Y.H.X. and M.R.X. performed data quality control; G.L.G., Y.C.B., P.D.C., R.C., Y.C., T.L.C., J.L.C., Y.Q.C., Z.J.D., Y.D., Y.Y.D., Q.D., J.H.G., Q.Y.G., Y.H., Z.Z.H., C.C.H., R.W.H., L.J.L., C.P.L., Q.X.L., B.S.L., C.L., N.Y.L., Y.L., J.L., L.L.M., W.W.M., S.Z.Q., J.Q., T.M.S., S.P.T., Y.Q.T., S.T., D.W.W., F.W., J.L.W., P.W., X.Q.W., Y.P.W., D.T.W., Y.K.W., P.X., X.F.X., L.Y.Y., H.B.Z., X.Z., G.Z., Y.T.Z., S.Y.Z collected a subset of the data for this study. L.L.S. and Y.H. wrote the manuscript. All authors reviewed the final manuscript.

Reference

1. Sporns, O., Tononi, G. & Kotter, R. The human connectome: A structural description of the human brain. *PLoS Comput Biol* **1**, e42 (2005).
2. Smith, S.M.*, et al.* Functional connectomics from resting-state fMRI. *Trends Cogn Sci* **17**, 666-682 (2013).
3. Park, H.J. & Friston, K. Structural and functional brain networks: from connections to cognition. *Science* **342**, 1238411 (2013).
4. Bassett, D.S. & Sporns, O. Network neuroscience. *Nat Neurosci* **20**, 353-364 (2017).
5. Biswal, B., Yetkin, F.Z., Haughton, V.M. & Hyde, J.S. Functional connectivity in the motor cortex of resting human brain using echo-planar MRI. *Magn Reson Med* **34**, 537-541 (1995).
6. Zuo, X.N.*, et al.* Human Connectomics across the Life Span. *Trends Cogn Sci* **21**, 32-45 (2017).
7. Gao, W., Lin, W., Grewen, K. & Gilmore, J.H. Functional Connectivity of the Infant Human Brain: Plastic and Modifiable. *Neuroscientist* **23**, 169-184 (2017).
8. Cao, M., Huang, H. & He, Y. Developmental Connectomics from Infancy through Early Childhood. *Trends Neurosci* **40**, 494-506 (2017).
9. Keunen, K., Counsell, S.J. & Benders, M. The emergence of functional architecture during early brain development. *Neuroimage* **160**, 2-14 (2017).
10. Di Martino, A.*, et al.* Unraveling the miswired connectome: a developmental perspective. *Neuron* **83**, 1335-1353 (2014).
11. Ecker, C., Bookheimer, S.Y. & Murphy, D.G.M. Neuroimaging in autism spectrum disorder: brain structure and function across the lifespan. *The Lancet Neurology* **14**, 1121-1134 (2015).
12. Di Martino, A.*, et al.* Shared and distinct intrinsic functional network centrality in autism and attention-deficit/hyperactivity disorder. *Biol Psychiatry* **74**, 623-632 (2013).
13. Perovnik, M., Rus, T., Schindlbeck, K.A. & Eidelberg, D. Functional brain networks in the evaluation of patients with neurodegenerative disorders. *Nat Rev Neurol* **19**, 73-90 (2023).
14. Chai, Y.*, et al.* Functional connectomics in depression: insights into therapies. *Trends Cogn Sci* (2023).
15. Fornito, A., Zalesky, A. & Breakspear, M. The connectomics of brain disorders. *Nat Rev Neurosci* **16**, 159-172 (2015).
16. Gong, Q. & He, Y. Depression, neuroimaging and connectomics: a selective overview. *Biol Psychiatry* **77**, 223-235 (2015).
17. Cole, T.J. The development of growth references and growth charts. *Ann Hum Biol* **39**, 382-394 (2012).
18. Bethlehem, R.A.I.*, et al.* Brain charts for the human lifespan. *Nature* (2022).
19. Rutherford, S., *et al.* Charting brain growth and aging at high spatial precision. *Elife* (2021).
20. Chen, L.Z., Holmes, A.J., Zuo, X.N. & Dong, Q. Neuroimaging brain growth charts: A road to mental health. *Psychoradiology* **1**, 272-286 (2021).
21. Deery, H.A., Di Paolo, R., Moran, C., Egan, G.F. & Jamadar, S.D. The older adult brain is less modular, more integrated, and less efficient at rest: A systematic review of large-scale resting-state functional brain networks in aging. *Psychophysiology* **60**, e14159 (2023).
22. Edde, M., Leroux, G., Altena, E. & Chanraud, S. Functional brain connectivity changes across the human life span: From fetal development to old age. *J Neurosci Res* **99**, 236-262 (2021).
23. Biswal, B.B.*, et al.* Toward discovery science of human brain function. *Proc Natl Acad Sci U S A* **107**, 4734-4739 (2010).
24. Betzel, R.F.*, et al.* Changes in structural and functional connectivity among resting-state networks across the human lifespan. *Neuroimage* **102 Pt 2**, 345-357 (2014).
25. Cao, M.*, et al.* Topological organization of the human brain functional connectome across the lifespan. *Dev Cogn Neurosci* **7**, 76-93 (2014).
26. Chen, Y.*, et al.* Age-related early/late variations of functional connectivity across the human lifespan. *Neuroradiology* **60**, 403-412 (2018).
27. Petrican, R., Taylor, M.J. & Grady, C.L. Trajectories of brain system maturation from childhood to older adulthood: Implications for lifespan cognitive functioning. *Neuroimage* **163**, 125-149 (2017).
28. Vij, S.G., Nomi, J.S., Dajani, D.R. & Uddin, L.Q. Evolution of spatial and temporal features of functional brain networks across the lifespan. *Neuroimage* **173**, 498-508 (2018).
29. Wang, L., Su, L., Shen, H. & Hu, D. Decoding lifespan changes of the human brain using resting-state functional connectivity MRI. *PLoS One* **7**, e44530 (2012).
30. Fjell, A.M.*, et al.* Relationship between structural and functional connectivity change across the adult lifespan: A longitudinal investigation. *Hum Brain Mapp* **38**, 561-573 (2017).

31. Luo, A., *et al.* Functional Connectivity Development along the Sensorimotor-Association Axis Enhances the Cortical Hierarchy. *BioRxiv* (2023).
32. Wu, K., *et al.* Topological organization of functional brain networks in healthy children: differences in relation to age, sex, and intelligence. *PLoS One* **8**, e55347 (2013).
33. Gu, S., *et al.* Emergence of system roles in normative neurodevelopment. *Proc Natl Acad Sci U S A* **112**, 13681-13686 (2015).
34. Sanders, A.F.P., *et al.* Age-related differences in resting-state functional connectivity from childhood to adolescence. *Cereb Cortex* (2023).
35. Sherman, L.E., *et al.* Development of the Default Mode and Central Executive Networks across early adolescence: A longitudinal study. *Developmental Cognitive Neuroscience* **10**, 148-159 (2014).
36. Marek, S., Hwang, K., Foran, W., Hallquist, M.N. & Luna, B. The Contribution of Network Organization and Integration to the Development of Cognitive Control. *PLoS Biol* **13**, e1002328 (2015).
37. Borghi, E., *et al.* Construction of the World Health Organization child growth standards: selection of methods for attained growth curves. *Stat Med* **25**, 247-265 (2006).
38. D. Mikis Stasinopoulos, R.A.R. Generalized Additive Models for Location Scale and Shape (GAMLSS) in R. *Journal of Statistical Software* **23** (2007).
39. Peterson, M.R., *et al.* Normal childhood brain growth and a universal sex and anthropomorphic relationship to cerebrospinal fluid. *J Neurosurg Pediatr* **28**, 458-468 (2021).
40. Zhang, H., *et al.* Growth charts of brain morphometry for preschool children. *Neuroimage* **255**, 119178 (2022).
41. Dong, H.-M., *et al.* Charting brain growth in tandem with brain templates at school age. *Science Bulletin* **65**, 1924-1934 (2020).
42. Gordon, E.M., *et al.* Precision Functional Mapping of Individual Human Brains. *Neuron* **95**, 791-807 e797 (2017).
43. Li, M., *et al.* Performing group-level functional image analyses based on homologous functional regions mapped in individuals. *PLoS Biol* **17**, e2007032 (2019).
44. Kong, R., *et al.* Spatial Topography of Individual-Specific Cortical Networks Predicts Human Cognition, Personality, and Emotion. *Cereb Cortex* **29**, 2533-2551 (2019).
45. Cui, Z., *et al.* Individual Variation in Functional Topography of Association Networks in Youth. *Neuron* (2020).
46. Bijsterbosch, J.D., *et al.* The relationship between spatial configuration and functional connectivity of brain regions. *Elife* **7** (2018).
47. Molloy, M.F. & Saygin, Z.M. Individual variability in functional organization of the neonatal brain. *Neuroimage* **253**, 119101 (2022).
48. Eyre, M., *et al.* The Developing Human Connectome Project: typical and disrupted perinatal functional connectivity. *Brain* **144**, 2199-2213 (2021).
49. Thomason, M.E., *et al.* Age-related increases in long-range connectivity in fetal functional neural connectivity networks in utero. *Dev Cogn Neurosci* **11**, 96-104 (2015).
50. Gao, W., *et al.* Functional Network Development During the First Year: Relative Sequence and Socioeconomic Correlations. *Cereb Cortex* **25**, 2919-2928 (2015).
51. Gao, W., *et al.* The synchronization within and interaction between the default and dorsal attention networks in early infancy. *Cereb Cortex* **23**, 594-603 (2013).
52. Sylvester, C.M., *et al.* Network-specific selectivity of functional connections in the neonatal brain. *Cereb Cortex* **33**, 2200-2214 (2023).
53. Grayson, D.S. & Fair, D.A. Development of large-scale functional networks from birth to adulthood: A guide to the neuroimaging literature. *Neuroimage* **160**, 15-31 (2017).
54. Yeo, B.T., *et al.* The organization of the human cerebral cortex estimated by intrinsic functional connectivity. *J Neurophysiol* **106**, 1125-1165 (2011).
55. Wang, D., *et al.* Parcellating cortical functional networks in individuals. *Nature Neuroscience* **18**, 1853-1860 (2015).
56. Brennan, B.P., *et al.* Use of an Individual-Level Approach to Identify Cortical Connectivity Biomarkers in Obsessive-Compulsive Disorder. *Biol Psychiatry Cogn Neurosci Neuroimaging* **4**, 27-38 (2019).
57. Cui, W., *et al.* Personalized fMRI Delineates Functional Regions Preserved within Brain Tumors. *Ann Neurol* **91**, 353-366 (2022).
58. Li, M., *et al.* Individualized functional connectome identified generalizable biomarkers for psychiatric symptoms in transdiagnostic patients. *Neuropsychopharmacology* **48**, 633-641 (2023).
59. Chan, M.Y., Park, D.C., Savalia, N.K., Petersen, S.E. & Wig, G.S. Decreased segregation of brain systems

across the healthy adult lifespan. *Proc Natl Acad Sci U S A* **111**, E4997-5006 (2014).
60. Xia, M., Wang, J. & He, Y. BrainNet Viewer: a network visualization tool for human brain connectomics. *PLoS One* **8**, e68910 (2013).
61. Huntenburg, J.M., Bazin, P.L. & Margulies, D.S. Large-Scale Gradients in Human Cortical Organization. *Trends Cogn Sci* **22**, 21-31 (2018).
62. Sydnor, V.J.*, et al.* Neurodevelopment of the association cortices: Patterns, mechanisms, and implications for psychopathology. *Neuron* (2021).
63. Xia, Y.*, et al.* Development of functional connectome gradients during childhood and adolescence. *Science Bulletin* (2022).
64. Pines, A.R.*, et al.* Dissociable multi-scale patterns of development in personalized brain networks. *Nat Commun* **13**, 2647 (2022).
65. Alexander-Bloch, A.F.*, et al.* On testing for spatial correspondence between maps of human brain structure and function. *Neuroimage* **178**, 540-551 (2018).
66. Kaczkurkin, A.N., Raznahan, A. & Satterthwaite, T.D. Sex differences in the developing brain: insights from multimodal neuroimaging. *Neuropsychopharmacology* **44**, 71-85 (2019).
67. Cahill, L. Why sex matters for neuroscience. *Nat Rev Neurosci* **7**, 477-484 (2006).
68. Zhang, C.*, et al.* Sex and Age Effects of Functional Connectivity in Early Adulthood. *Brain Connect* **6**, 700-713 (2016).
69. Dorfschmidt, L.*, et al.* Sexually divergent development of depression-related brain networks during healthy human adolescence. *Science Advances* **8**, eabm7825 (2022).
70. Sun, X.*, et al.* Mapping Neurophysiological Subtypes of Major Depressive Disorder Using Normative Models of the Functional Connectome. *Biol Psychiatry* (2023).
71. Wolfers, T.*, et al.* Mapping the Heterogeneous Phenotype of Schizophrenia and Bipolar Disorder Using Normative Models. *JAMA Psychiatry* **75**, 1146-1155 (2018).
72. Rutherford, S.*, et al*. Evidence for embracing normative modeling. *Elife* (2023).
73. Segal, A.*, et al.* Regional, circuit and network heterogeneity of brain abnormalities in psychiatric disorders. *Nat Neurosci* (2023).
74. Marquand, A.F., Rezek, I., Buitelaar, J. & Beckmann, C.F. Understanding Heterogeneity in Clinical Cohorts Using Normative Models: Beyond Case-Control Studies. *Biol Psychiatry* **80**, 552-561 (2016).
75. Tian, Y.E.*, et al.* Evaluation of Brain-Body Health in Individuals With Common Neuropsychiatric Disorders. *JAMA Psychiatry* **80**, 567-576 (2023).
76. Tian, Y.E.*, et al.* Heterogeneous aging across multiple organ systems and prediction of chronic disease and mortality. *Nat Med* (2023).
77. van den Heuvel, M.I. & Thomason, M.E. Functional Connectivity of the Human Brain in Utero. *Trends Cogn Sci* **20**, 931-939 (2016).
78. Raz, G. & Saxe, R. Learning in Infancy Is Active, Endogenously Motivated, and Depends on the Prefrontal Cortices. *Annual Review of Developmental Psychology* **2**, 247-268 (2020).
79. Gao, W. Evidence on the emergence of the brain's default network from 2-week-old to 2-year-old healthy pediatric subjects. *PNAS* (2009).
80. Fjell, A.M.*, et al.* What is normal in normal aging? Effects of aging, amyloid and Alzheimer's disease on the cerebral cortex and the hippocampus. *Prog Neurobiol* **117**, 20-40 (2014).
81. Pascoal, T.A.*, et al.* Abeta-induced vulnerability propagates via the brain's default mode network. *Nat Commun* **10**, 2353 (2019).
82. Wales, R.M. & Leung, H.-C.J.B.C. The effects of amyloid and tau on functional network connectivity in older populations. **11**, 599-612 (2021).
83. Jagust, W. Imaging the evolution and pathophysiology of Alzheimer disease. *Nat Rev Neurosci* **19**, 687-700 (2018).
84. Bedford, S.A., Seidlitz, J. & Bethlehem, R.A.I. Translational potential of human brain charts. *Clin Transl Med* **12**, e960 (2022).
85. Zhou, Z.X., Chen, L.Z., Milham, M.P., Zuo, X.N. & Lifespan Brain Chart, C. Six cornerstones for translational brain charts. *Sci Bull (Beijing)* (2023).
86. Cash, R.F.H., Cocchi, L., Lv, J., Fitzgerald, P.B. & Zalesky, A. Functional magnetic resonance imaging–guided personalization of transcranial magnetic stimulation treatment for depression. *JAMA psychiatry* **78**, 337-339 (2021).
87. Lotter, L.D.*, et al.* Human cortex development is shaped by molecular and cellular brain systems. *bioRxiv* (2023).
88. Brouwer, R.M.*, et al.* Genetic variants associated with longitudinal changes in brain structure across the

lifespan. *Nat Neurosci* **25**, 421-432 (2022).
89. Kopal, J., Uddin, L.Q. & Bzdok, D. The end game: respecting major sources of population diversity. *Nat Methods* (2023).
90. Di Biase, M.A.*, et al.* Mapping human brain charts cross-sectionally and longitudinally. *Proc Natl Acad Sci U S A* **120**, e2216798120 (2023).
91. Elyounssi, S.*, et al.* Uncovering and mitigating bias in large, automated MRI analyses of brain development. *bioRxiv* (2023).
92. Esteban, O.*, et al.* MRIQC: Advancing the automatic prediction of image quality in MRI from unseen sites. *PLoS One* **12**, e0184661 (2017).
93. Rosen, A.F.G.*, et al.* Quantitative assessment of structural image quality. *Neuroimage* **169**, 407-418 (2018).
94. Wang, L.*, et al.* Benchmark on Automatic 6-month-old Infant Brain Segmentation Algorithms: The iSeg-2017 Challenge. *IEEE Trans Med Imaging* (2019).
95. Zeng, Z.*, et al.* 3D-MASNet: 3D mixed-scale asymmetric convolutional segmentation network for 6-month-old infant brain MR images. *Human Brain Mapping* (2022).
96. Glasser, M.F.*, et al.* The minimal preprocessing pipelines for the Human Connectome Project. *Neuroimage* **80**, 105-124 (2013).
97. Ji, J.L.*, et al.* QuNex—An integrative platform for reproducible neuroimaging analytics. *Frontiers in Neuroinformatics* **17** (2023).
98. Feczko, E.*, et al.* Adolescent Brain Cognitive Development (ABCD) Community MRI Collection and Utilities. (2021).
99. Makropoulos, A.*, et al.* The developing human connectome project: A minimal processing pipeline for neonatal cortical surface reconstruction. *Neuroimage* **173**, 88-112 (2018).
100. Wang, L.*, et al.* iBEAT V2.0: a multisite-applicable, deep learning-based pipeline for infant cerebral cortical surface reconstruction. *Nat Protoc* (2023).
101. Williams, L.Z.J.*, et al.* Structural and functional asymmetry of the neonatal cerebral cortex. *Nat Hum Behav* (2023).
102. Wu, Z.*, et al.* Construction of 4D infant cortical surface atlases with sharp folding patterns via spherical patch-based group-wise sparse representation. *Hum Brain Mapp* **40**, 3860-3880 (2019).
103. Fitzgibbon, S.P.*, et al.* The developing Human Connectome Project (dHCP) automated resting-state functional processing framework for newborn infants. *Neuroimage* **223**, 117303 (2020).
104. Eickhoff, S.B., Yeo, B.T.T. & Genon, S. Imaging-based parcellations of the human brain. *Nat Rev Neurosci* **19**, 672-686 (2018).
105. Buckner, R.L., Krienen, F.M., Castellanos, A., Diaz, J.C. & Yeo, B.T. The organization of the human cerebellum estimated by intrinsic functional connectivity. *J Neurophysiol* **106**, 2322-2345 (2011).
106. Mueller, S.*, et al.* Individual variability in functional connectivity architecture of the human brain. *Neuron* **77**, 586-595 (2013).
107. Sun, L.*, et al.* Structural insight into the individual variability architecture of the functional brain connectome. *Neuroimage*, 119387 (2022).
108. Johnson, W.E., Li, C. & Rabinovic, A. Adjusting batch effects in microarray expression data using empirical Bayes methods. *Biostatistics* **8**, 118-127 (2007).
109. Pomponio, R.*, et al.* Harmonization of large MRI datasets for the analysis of brain imaging patterns throughout the lifespan. *Neuroimage* **208**, 116450 (2020).
110. Hu, F.*, et al.* Image harmonization: A review of statistical and deep learning methods for removing batch effects and evaluation metrics for effective harmonization. *Neuroimage* **274**, 120125 (2023).
111. Dunn, P.K. & Smyth, G.K. Randomized Quantile Residuals. *Journal of Computational and Graphical Statistics* **5**, 236-244 (1996).

Supplementary Materials

Supplementary tables:

Supplementary Table 1. Demographic and scanner details of each dataset (available in separate file)

Supplementary Table 2. The detailed information of the age range, number of participants, and sex ratio for each atlas (available in separate file)

Supplementary figures:

Supplementary Figure 1. The quality control framework of imaging data

Supplementary Figure 2. Schematic overview of the cortical surface registration

Supplementary Figure 3. Schematic overview of the system-level atlas construction

Supplementary Figure 4. The life-cycle set of population-level cortical functional atlases from 32 postmenstrual weeks to 80 years

Supplementary Figure 5. The reference atlas used for comparison

Supplementary Figure 6. The lifespan trajectories of within-system and between-system functional connectivity

Supplementary Figure 7. Sex-stratified normative trajectories of the functional connectome

Supplementary Figure 8. Distribution of the number of metrics per patient with extremely deviations

Supplementary Figure 9. Bayesian information criterion for each family of distributions of whole-brain global metrics

Supplementary Figure 10. Bayesian information criterion for model selection of whole-brain global metrics

Supplementary Figure 11. Residual distribution plots from the GAMLSS model of four whole-brain functional metrics

Supplementary Figure 12. Detrended transformed Owen's plots from the GAMLSS model of whole-brain functional metrics

Supplementary Figure 13. The GAMLSS trajectories excluding the ABCD study or the UK Biobank study

Supplementary Figure 14. Bootstrap-derived 95% CI for normative trajectories of whole-brain functional metrics

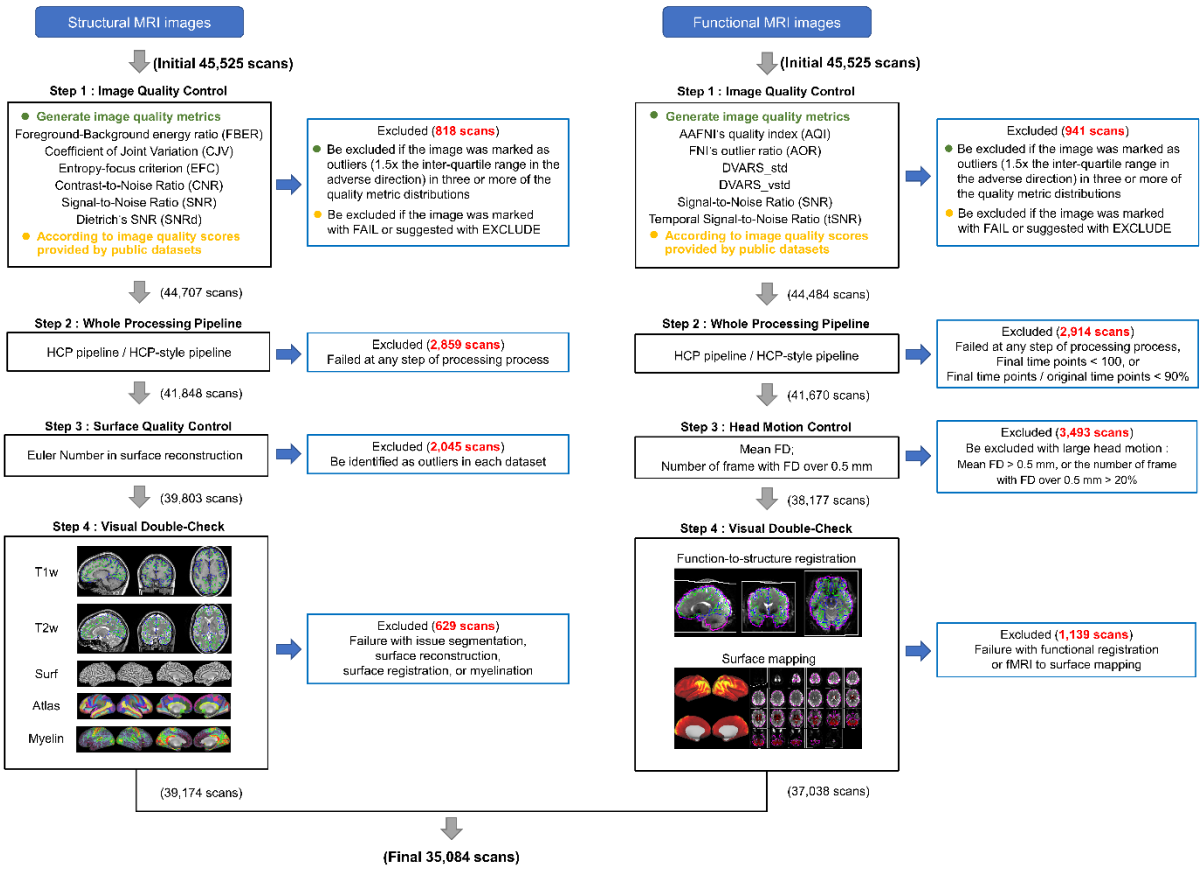

***Supplementary Figure 1*. The quality control framework of imaging data.** Applying the rigorous four-step quality control process led to the total exclusion of 10,441 scans from 9774 subjects. The final sample comprised 35,084 scans with high-quality functional and structural images, including 33,809 scans (N = 32,328) from healthy controls (HCs), 653 scans (N = 653) from patients with ASD, and 622 scans (N = 622) from patients with MDD.

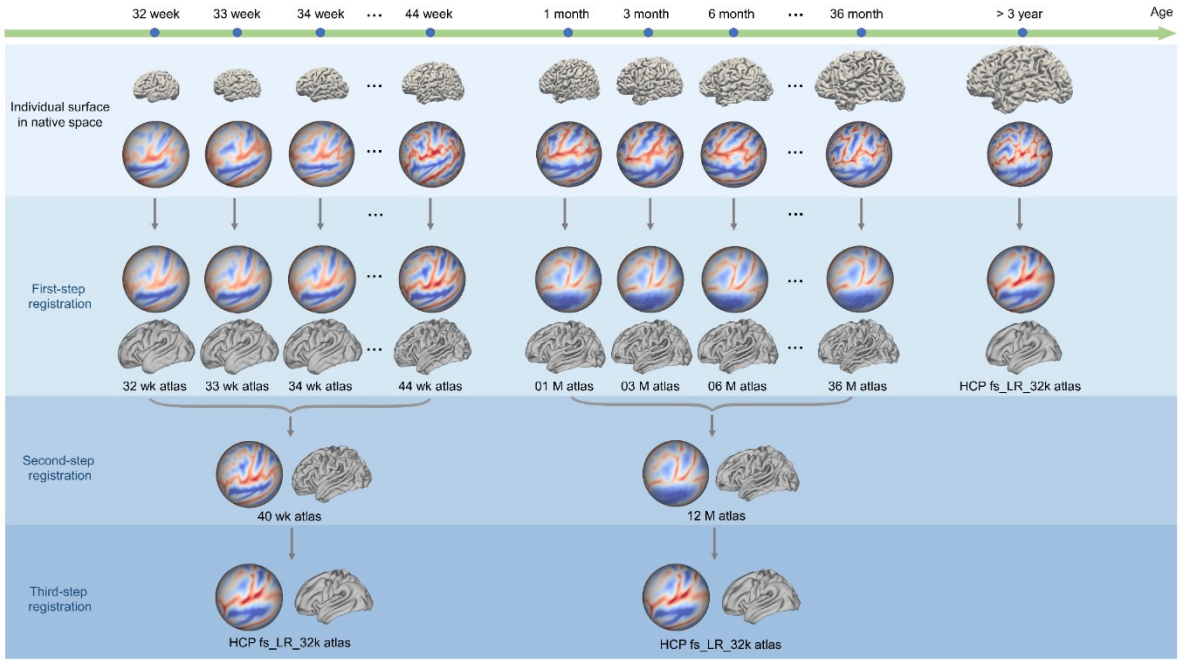

***Supplementary Figure 2*. Schematic overview of the cortical surface registration.** The surface registration process aimed for precise alignment with the fs_LR_32k standard space. For participants aged 32 to 44 postmenstrual weeks, a three-step procedure was employed: (1) individual surfaces were mapped to their corresponding postmenstrual week templates; (2) the 32-39 and 41-44 postmenstrual week templates were registered to the 40-week template [1]; and (3) the 40-week template was registered to the fs_LR_32k surface template. For participants aged 0-36 months: (1) surfaces were aligned with their monthly age templates [2]; (2) all monthly templates were registered into the 12-month template; and (3) this 12-month template was then mapped to the fs_LR_32k surface template. For participants aged three years and older, the individual surfaces were mapped to the fs_LR_32k space. The transformations involving adult templates — from individual to fsaverage space, then from fsaverage space to Conte69 space, and finally downsampled to the fs_LR_32k space — are not illustrated in the figure. wk, week; M, month.

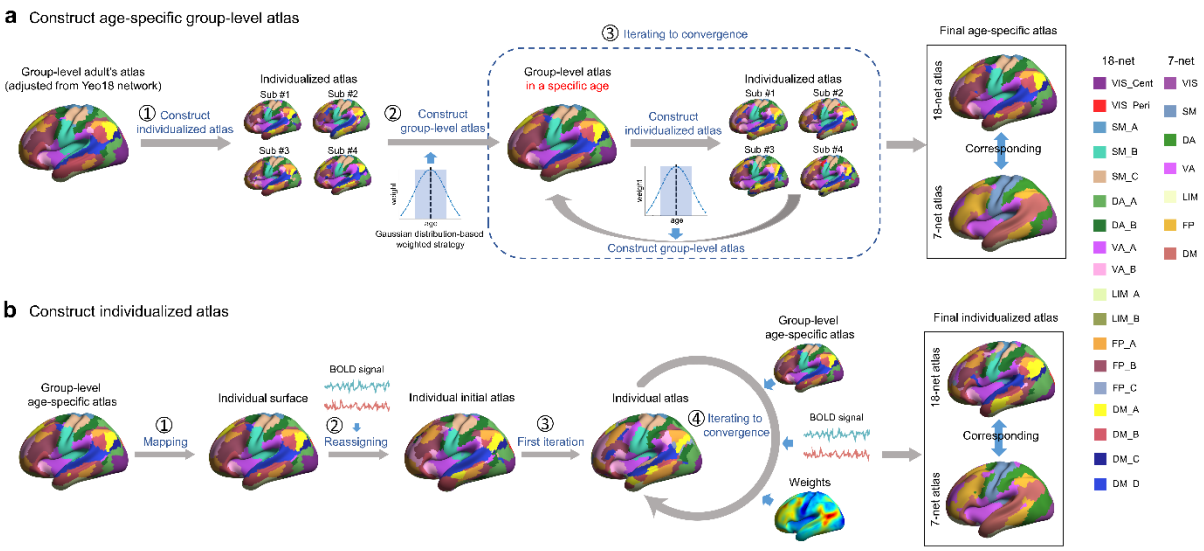

Supplementary Figure 3. **Schematic overview of the system-level atlas construction. a,** Population-level age-specific atlas construction. We segmented individuals' ages into 26 intervals and constructed 26 developmental atlases, ranging from 32 weeks postmenstrual age to 80 years. For a given age interval, the atlas generation process involved the following steps. (1) Constructing an individualized atlas: we used an individualized parcellation iteration algorithm to map the adult 18-network atlas to each participant. (2) Constructing a population-level atlas: we introduced a population-level atlas generation method based on a Gaussian probability distribution. We assigned weights to each participant based on their age's position within a Gaussian distribution (mean $\mu = 0$ and standard deviation $\sigma = 1$). The weight quantified the participant's contribution to the population-level atlas construction, with proximity to the target age of atlas resulting in a greater contribution. For each cortical vertex, we calculated the across-participant cumulative probability belonging to each network, and assigned vertex labels to the network with the highest cumulative probability, resulting in an initial age-specific population-level atlas. (3) Iteration to convergence: we iteratively repeated steps 1 and 2 until the overlap between the current and previous atlases exceeded 95% or the total number of iterations surpassed 10, indicating convergence. Finally, according to the correspondence between 18 and 7 networks, we obtained the age-specific 7-network atlas as well. **b**, Individualized atlas construction (reproduced from [3]). (1) Personalized mapping and reference establishment: the age-specific population-level atlas was mapped onto an individual participant's cortical surface. The mean BOLD signal time series of a network was averaged across its vertices, providing atlas-based reference signals essential for the upcoming optimization phase. (2) Correlation and vertex reassignment: for a given vertex, the BOLD signal underwent a correlation analysis with the 18 reference signals. The network with the highest correlation was assigned to this vertex. (3) Signal averaging and iterative refinement: a combined reference signal was generated by weighted averaging the signal from step (2) and the initial reference signals from step (1). Factors influencing this averaging included intersubject variability, tSNR, and iteration counts. This combined signal then served as an updated reference, guiding the reassignment of brain vertices to their most suitable networks. (4) Iterative convergence: the procedures in steps (2) and (3) were iteratively executed until reaching a predefined stopping criterion (the overlap between the

current and previous atlases exceeded 98%, or the total number of iterations surpassed 50). More information on this iterative functional parcellation approach can be found in the study by Wang and colleagues [3]. VIS, visual; SM, somatomotor; DA, dorsal attention; VA, ventral attention; LIM, limbic; FP, frontoparietal; DM, default mode.

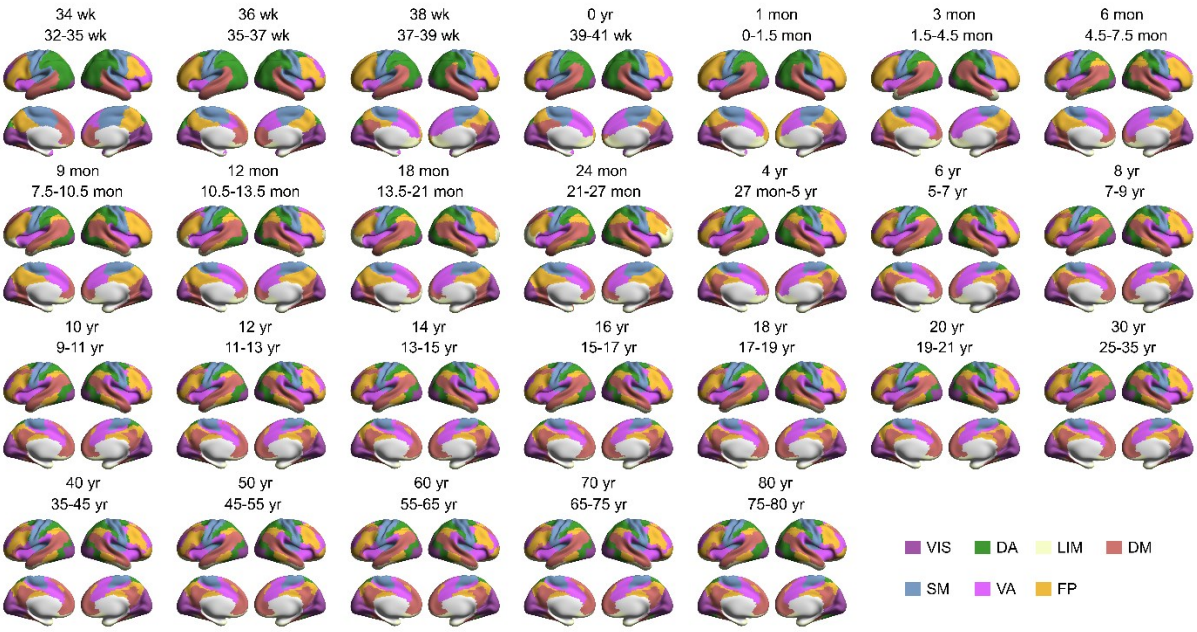

Supplementary Figure 4. **The life-cycle set of population-level cortical functional atlases from 32 postmenstrual weeks to 80 years.** VIS, visual; SM, somatomotor; DA, dorsal attention; VA, ventral attention; LIM, limbic; FP, frontoparietal; DM, default mode. wk, week; mon, month; yr, year.

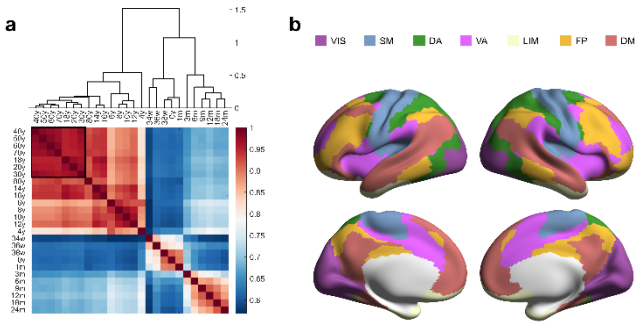

Supplementary Figure 5. **The reference atlas used for comparison. a**, Hierarchical clustering on the 26×26 atlas similarity matrix. The atlas similarity was defined as the degree of vertex label overlap between two atlases. For instance, if there were 4,000 vertices with the same label, the similarity of these two atlases was 4,000/4,661 = 0.86. **b**, The reference atlas. We selected the relatively congruent group of atlases, including the 18-, 20-, 30-, 40-, 50-, 60-, and 70-year atlases. For each vertex, we assigned the label as the system that exhibited the highest occurrence probability across these seven atlases, generating the final 7-network reference atlas. w, week; m, month; y, year.

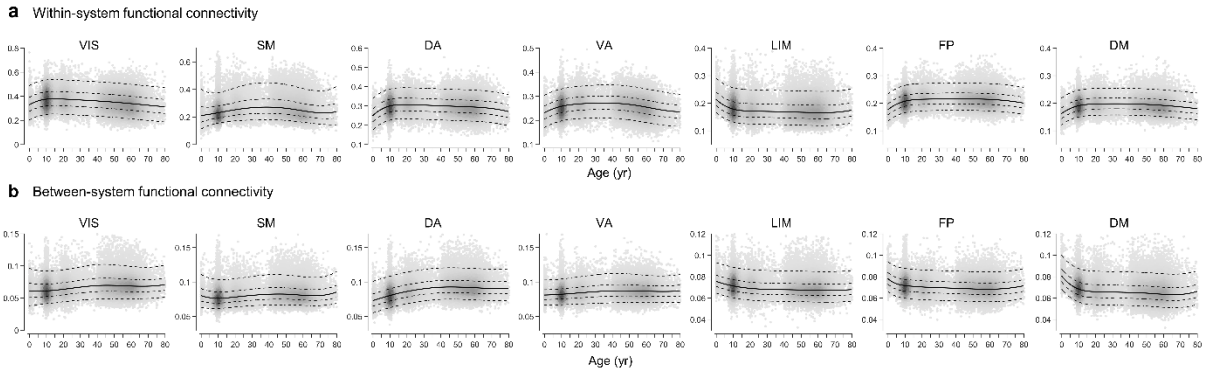

Supplementary Figure 6. **The lifespan trajectories of within-system and between-system functional connectivity. a,** Normative trajectory of within-system functional connectivity (FC) as estimated by GAMLSS. The median (50% centile) is represented by a solid line, while the 5%, 25%, 75%, and 95% centiles are indicated by dotted lines. b, Normative trajectory of between-system FC. VIS, visual; SM, somatomotor; DA, dorsal attention; VA, ventral attention; LIM, limbic; FP, frontoparietal; DM, default mode. wk, week; mon, month; yr, year.

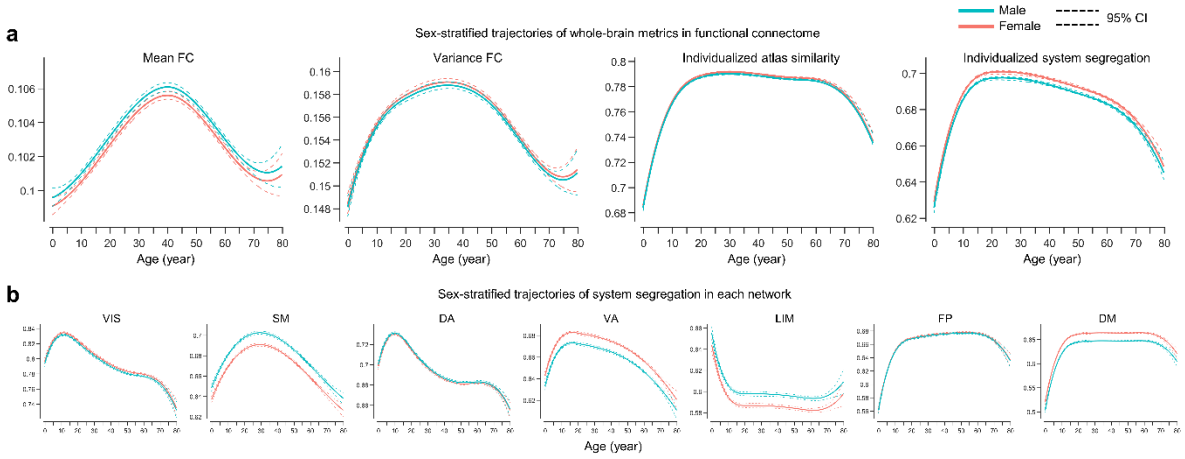

Supplementary Figure 7. **Sex-stratified normative trajectories of the functional connectome. a**, Sex-stratified normative trajectories for whole-brain metrics. The solid line represents the 50% centile, with the two surrounding dotted lines denoting the 95% CI. The subplots from left to right represent whole-brain mean functional connectivity (FC), variance FC, individualized atlas similarity, and system segregation, respectively. **b**, Sex-specific trajectories for system segregation across each network. VIS, visual; SM, somatomotor; DA, dorsal attention; VA, ventral attention; LIM, limbic; FP, frontoparietal; DM, default mode.

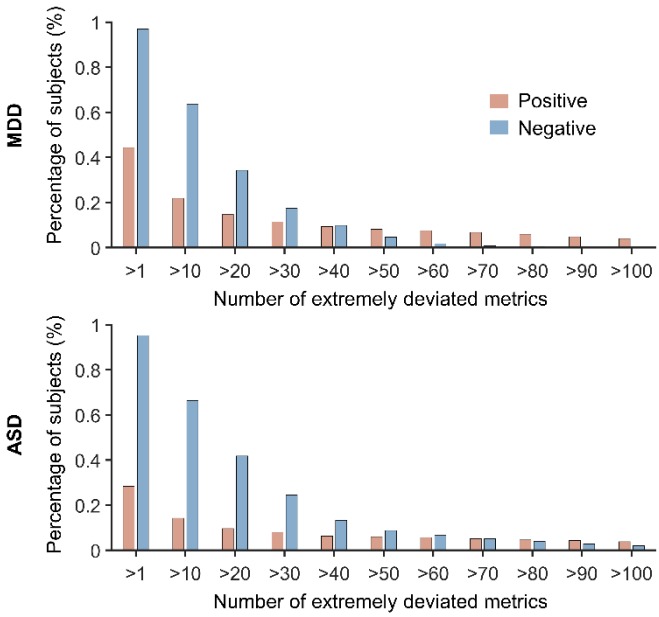

Supplementary Figure 8. **Distribution of the number of metrics per patient with extremely deviations.** The Bar plots show the percentage of subjects of the number of metrics with extremely positive (red) and negative (blue) deviations (top panel for MDD, bottom panel for ASD).

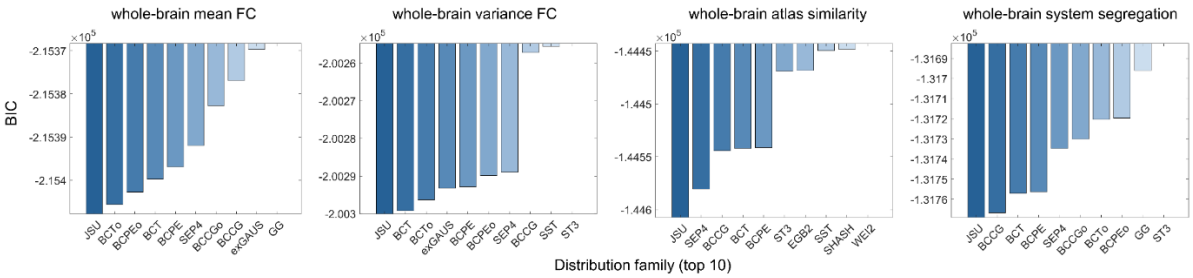

Supplementary Figure 9. **Bayesian information criterion for each family of distributions of whole-brain global metrics**. For each representative functional phenotype, the top ten distributions with the lowest Bayesian information criterion (BIC) values were visualized. Among the evaluated distributions, Johnson's Su (JSU) consistently outperformed others across all phenotypes. The JSU distribution has four parameters: median (μ), coefficient of variation (σ), skewness (ν), and kurtosis (τ). Distribution acronyms are in accordance with the GAMLSS package notation. FC, functional connectome.

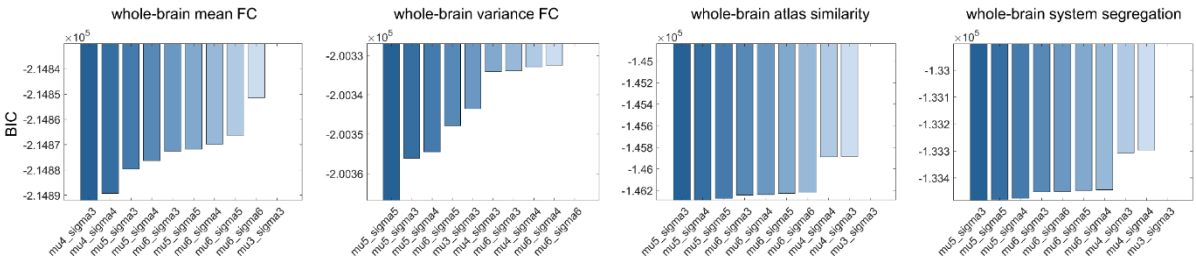

Supplementary Figure 10. **Bayesian information criterion for model selection of whole-brain global metrics**. Optimal df = 4 of location (μ) parameter and df = 3 of scale (σ) parameter for whole-brain mean functional connectivity; optimal df = 5 of location (μ) parameter and df = 5 of scale (σ) parameter for whole-brain variance functional connectivity; optimal df = 5 of location (μ) parameter and df = 3 of scale (σ) parameter for whole-brain atlas similarity; optimal df = 5 of location (μ) parameter and df = 3 of scale (σ) parameter for whole-brain system segregation.

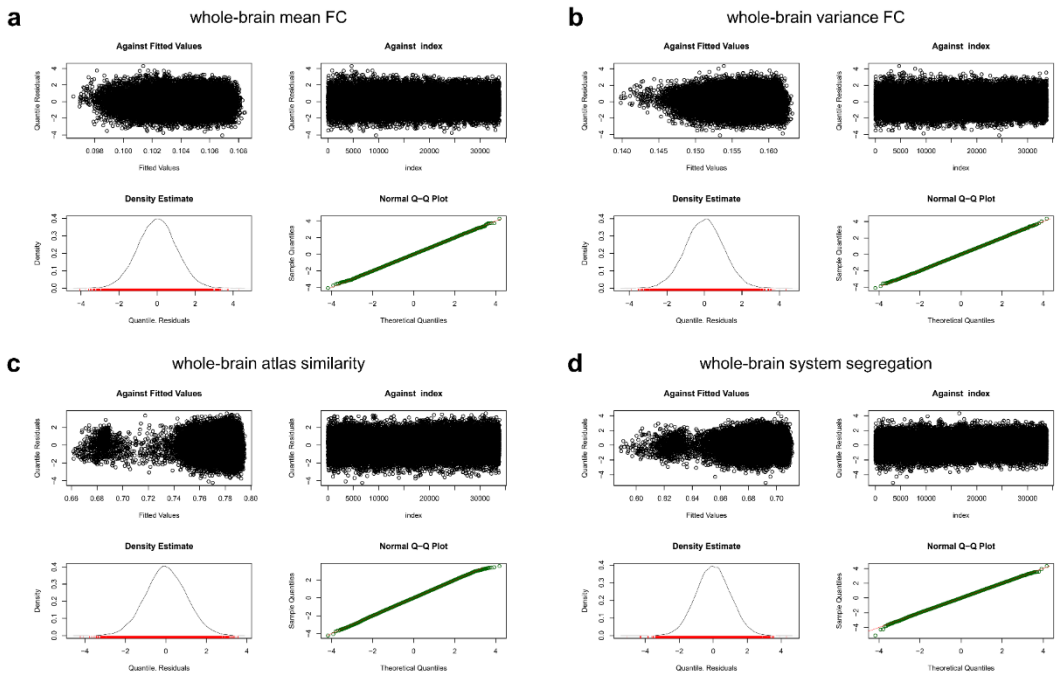

Supplementary Figure 11. **Residual distribution plots from the GAMLSS model of four whole-brain functional metrics.** The plots showed that the model residuals of whole-brain mean functional connectivity (**a**), variance functional connectivity (**b**), atlas similarity (**c**), and system segregation (**d**) were normally distributed.

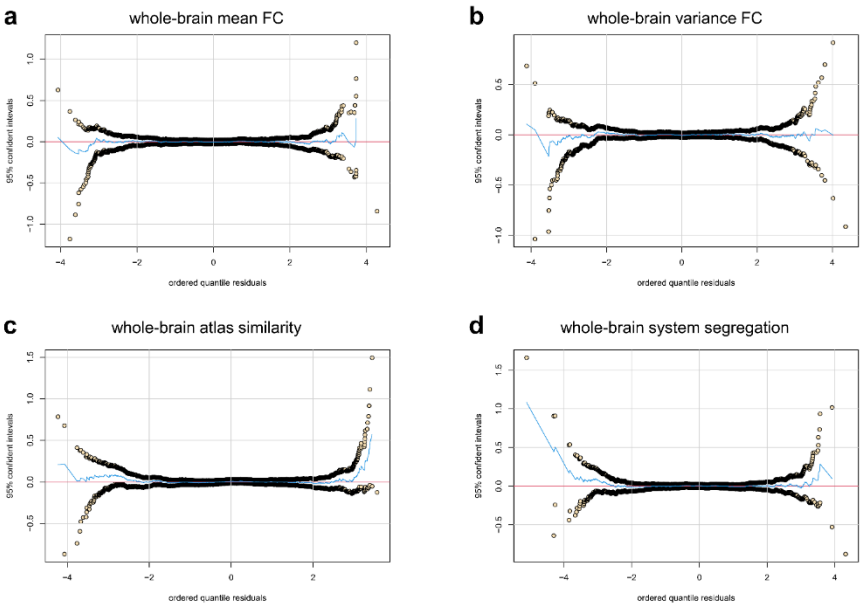

Supplementary Figure 12. **Detrended transformed Owen's plots from the GAMLSS model of whole-brain functional metrics.** The zero horizontal line is within the confidence intervals, suggesting that the residuals of whole-brain mean functional connectivity (**a**), variance functional connectivity (**b**), atlas similarity (**c**), and system segregation (**d**) follow a normal distribution.

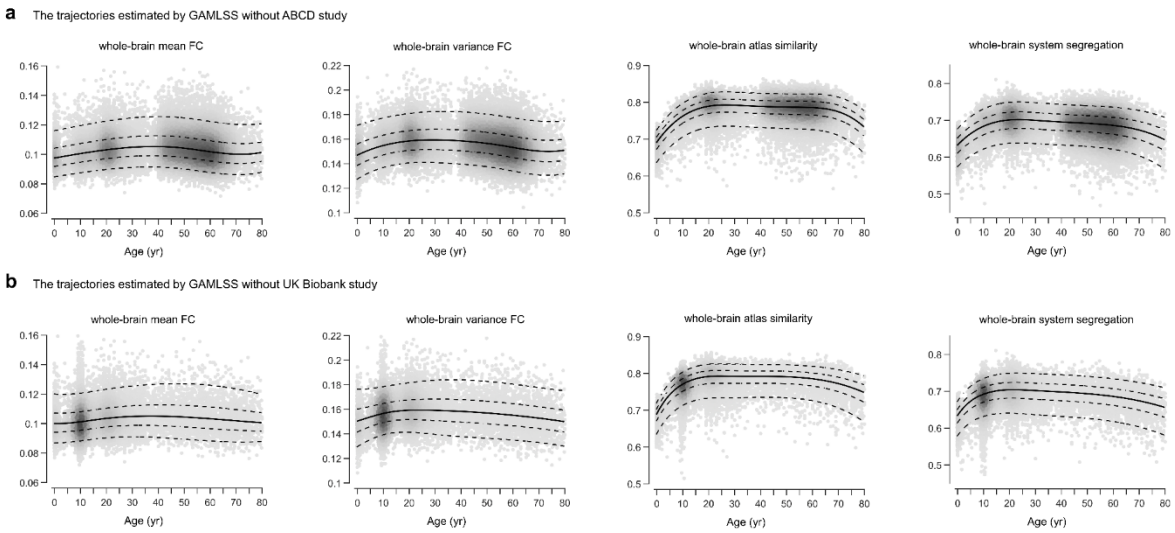

Supplementary Figure 13. **The GAMLSS trajectories excluding the ABCD study or the UK Biobank study. a**, Trajectories of whole-brain mean functional connectivity, variance functional connectivity, atlas similarity, and system segregation, excluding the ABCD study. **b**, Trajectories of whole-brain mean functional connectivity, variance functional connectivity, atlas similarity, and system segregation, excluding the UK Biobank study. The median (50% centile) is represented by a solid line, while the 5%, 25%, 75%, and 95% centiles are indicated by dotted lines.

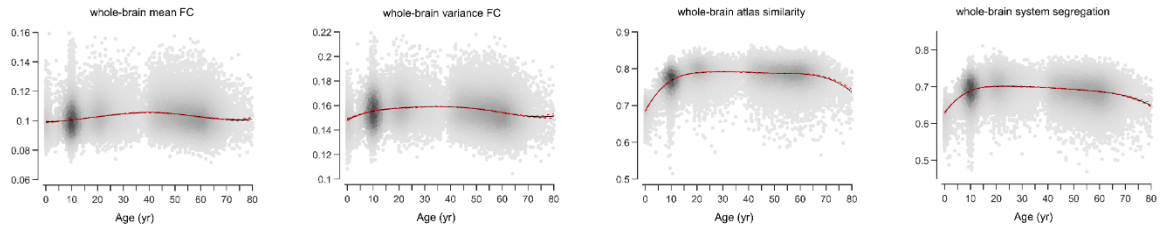

Supplementary Figure 14. **Bootstrap-derived 95% CI for normative trajectories of whole-brain functional metrics.** The bootstrap analysis included running 1000 bootstrap iterations with replacement sampling and conducting 1000 fitted GAMLSS models. From left to right, the plots depict the 95% CI (red dashed lines) for the median (50th percentile) trajectories (black solid line) of whole-brain mean functional connectivity, variance functional connectivity, atlas similarity, and system segregation, highlighting the robustness of the lifespan modeling framework.

Reference

1. Williams, L.Z.J., *et al.* Structural and functional asymmetry of the neonatal cerebral cortex. *Nat Hum Behav* (2023).

2. Wu, Z., *et al.* Construction of 4D infant cortical surface atlases with sharp folding patterns via spherical patch-based group-wise sparse representation. *Hum Brain Mapp* **40**, 3860-3880 (2019).

3. Wang, D., *et al.* Parcellating cortical functional networks in individuals. *Nature Neuroscience* **18**, 1853-1860 (2015).